AGU PUBLICATIONS

JGR

Journal of Geophysical Research: Solid Earth

RESEARCH ARTICLE
10.1002/2015JB011925

Great earthquakes in low strain rate continental interiors: An example from SE Kazakhstan

G. E. Campbell[1], R. T. Walker[2], K. Abdrakhmatov[3], J. Jackson[1], J. R. Elliott[2], D. Mackenzie[2], T. Middleton[2], and J.-L. Schwenninger[4]

[1]Bullard Laboratories, Department of Earth Sciences, University of Cambridge, Cambridge, UK, [2]Department of Earth Sciences, University of Oxford, Oxford, UK, [3]Kyrgyz Institute of Seismology, Bishkek, Kyrgyzstan, [4]Research Laboratory for Archaeology and the History of Art, University of Oxford, Oxford, UK

Key Points:
- The Lepsy fault is an E-W reverse right-lateral fault in the northern Tien Shan
- It has generated two substantial earthquakes (up to M_w 8) in the Holocene
- The fault connects a slowly deforming region to a faster deforming region

Correspondence to:
G. E. Campbell,
gc416@cam.ac.uk

Citation:
Campbell, G. E., R. T. Walker, K. Abdrakhmatov, J. Jackson, J. R. Elliott, D. Mackenzie, T. Middleton, and J.-L. Schwenninger (2015), Great earthquakes in low strain rate continental interiors: An example from SE Kazakhstan, *J. Geophys. Res. Solid Earth*, *120*, 5507–5534, doi:10.1002/2015JB011925.

Received 2 FEB 2015
Accepted 9 JUN 2015
Accepted article online 16 JUN 2015
Published online 6 AUG 2015

Abstract The Lepsy fault of the northern Tien Shan, SE Kazakhstan, extends E-W 120 km from the high mountains of the Dzhungarian Ala-tau, a subrange of the northern Tien Shan, into the low-lying Kazakh platform. It is an example of an active structure that connects a more rapidly deforming mountain region with an apparently stable continental region and follows a known Palaeozoic structure. Field-based and satellite observations reveal an ~10 m vertical offset exceptionally preserved along the entire length of the fault. Geomorphic analysis and age control from radiocarbon and optically stimulated luminescence dating methods indicate that the scarp formed in the Holocene and was generated by at least two substantial earthquakes. The most recent event, dated to sometime after ~400 years B.P., is likely to have ruptured the entire ~120 km fault length in a M_w 7.5–8.2 earthquake. The Lepsy fault kinematics were characterized using digital elevation models and high-resolution satellite imagery, which indicate that the predominant sense of motion is reverse right lateral with a fault strike, dip, and slip vector azimuth of ~110°, 50°S, and 317–343°, respectively, which is consistent with predominant N-S shortening related to the India-Eurasia collision. In light of these observations, and because the activity of the Lepsy fault would have been hard to ascertain if it had not ruptured in the recent past, we note that the absence of known active faults within low-relief and low strain rate continental interiors does not always imply an absence of seismic hazard.

1. Introduction

This paper looks at seismic hazard in regions that may contain active faults, but which have no documented record of earthquakes. Large-magnitude earthquakes are rare though widespread in apparently stable continental regions (SCRs) [*Sykes*, 1978; *Johnston and Kanter*, 1990; *Schulte and Mooney*, 2005; *Clark et al.*, 2012], and examples exist in parts of India, Australia, Africa, and North America [*Fuller*, 1912; *Everingham and Gregson*, 1969; *McCaffrey*, 1989; *Johnston and Schweig*, 1996; *Seeber et al.*, 1996; *Rajendran et al.*, 2001; *Copley et al.*, 2012]. Often, but not always, such events cause widespread destruction because of their size, because the damaging effects of shaking extend further from the source than in most continental regions, and because the faults on which they occur are often unknown.

In all of the examples of intraplate earthquakes listed above, long-term fault slip rates are relatively low (e.g., 1–2 mm/yr or less) compared with those in interplate regions or major collision boundaries within the continents (such as the Himalayan frontal thrust), and the recurrence times of large earthquakes on the majority of active faults within low strain rate regions are likely to exceed the length of the documented historical record. With repeat times of many thousands of years, erosion may also remove any clear expression of surface faulting from the landscape, creating additional challenges in identifying and characterizing seismogenic faults in slowly deforming continent interiors.

This paper is concerned with the foreland of the northern Tien Shan, central Asia (Figure 1). The Tien Shan itself is one of the worlds largest and most seismically active intracontinental orogens and accommodates up to 50% (15–20 mm/yr) of the total shortening related to the ongoing India-Eurasia collision [*Abdrakhmatov et al.*, 1996]. GPS velocities relative to stable Eurasia indicate that most of the shortening is concentrated within the mountain interior, which is where the majority of seismicity is confined (Figure 1). However, in the flat low-lying Kazakh platform, north of the Tien Shan, a few rare earthquakes of moderate size have occurred in

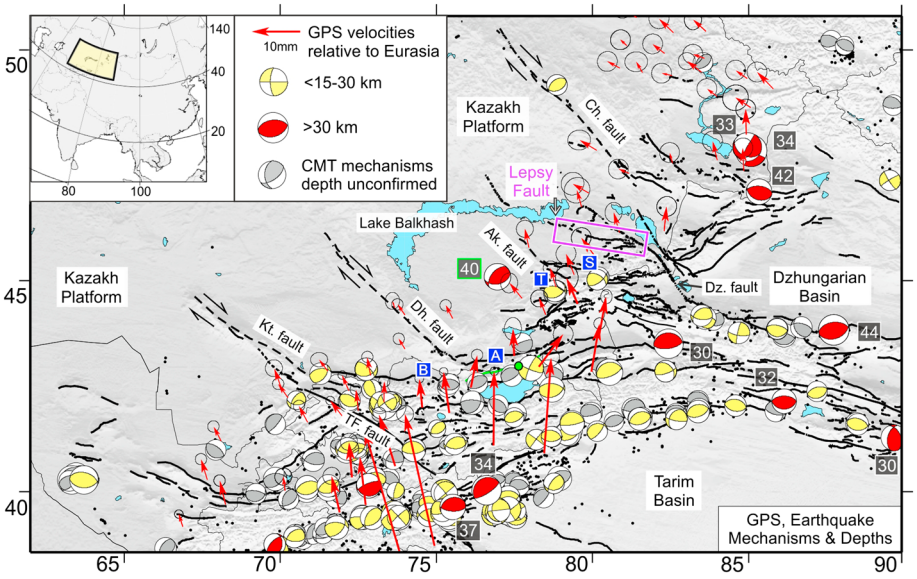

Figure 1. Active faults, earthquake mechanisms and centroid depths, and GPS velocities of the Tien Shan region. The purple box shows the Lepsy fault (Figure 2). Major NW-SE oriented platform faults are dashed in black, and currently, their activity in the Quaternary is unknown. Named from SW to NE, these include the Karatau (Kt.), Dzhalair-Naiman (Dh.), Aktas (Ak.), and Chingiz (Ch.) faults [after *Tapponnier and Molnar*, 1979]. The major NW-SE range interior/range-bounding strike-slip faults are the Talas-Ferghana fault (TF) [*Burtman et al.*, 1996] in the west and the Dzhungarian fault (Dz.) in the east [after *Voitovich*, 1969; *Tapponnier and Molnar*, 1979; *Campbell et al.*, 2013]. All other active faults are mapped from this study (from remote observations of satellite imagery and fieldwork) and existing studies [e.g., *Suvorov*, 1963; *Tapponnier and Molnar*, 1979; *Avouac et al.*, 1993; *Abdrakhmatov et al.*, 2001; *Thompson et al.*, 2002; *Arrowsmith et al.*, 2004]. The green dot marks part of the Chon-Kemin fault that ruptured in the 1911 M_s ~8.2 earthquake, with the fault zone itself shown as a green approximately E-W line. GPS velocities relative to stable Eurasia are shown [after *Zubovich et al.*, 2010]. Body waveform-modeled earthquakes are color coded by depth [after *Sloan et al.*, 2011, and references therein], with centroid depths ≥30 km indicated. Rare earthquakes occur in the platform, e.g., depth 40 km (depth outlined in green). Earthquakes in the updated *Engdahl et al.* [1998] catalogue are shown as black dots. Lettered blue squares mark the locations of major cities: Bishkek and Almaty (B and A, respectively) and major towns Taldykorgan and Sarkand (T and S, respectively). Country boundaries are shown as solid black lines.

recent decades (e.g., the 40 km depth event, outlined in green in Figure 1). GPS measurements indicate low though nonnegligible rates of shortening north of the Tien Shan (e.g., ≤2 mm/yr) [*Zubovich et al.*, 2010]. Due to the sparse seismicity, and overall absence of obvious geomorphic evidence of late Quaternary active faulting, the foreland of the northern Tien Shan is usually considered as a SCR or low strain rate continent interior, and it is not clear whether these rare foreland earthquakes occur on faults that connect with the active structures of the mountains and indeed whether the Kazakh platform may be susceptible to larger, more damaging, earthquakes than those present in instrumental catalogues.

The semiarid continental climate in the northern Tien Shan region has allowed exceptional preservation of historical earthquake ruptures, including the 1911 M_s ~8.2 Chon-Kemin surface rupture [*Bogdanovich et al.*, 1914; *Delvaux et al.*, 2001; *Abdrakhmatov et al.*, 2002] (with location marked by a green dot in Figure 1). We may therefore expect surface faulting associated with other, prehistoric, large earthquakes to be preserved in the landscape of this pristine environment. This paper examines the evidence for such an event on the Lepsy fault, in the Tien Shan forelands, and in an area that has no record of seismic activity. Identification and characterization of structures like the Lepsy fault are increasingly significant for hazard evaluation, especially given that it is only ~250 km NE from the highly populated former capital city of Kazakhstan, Almaty (Figure 1). The Lepsy fault is also only ~100 km from two significant administrative capitals, Sarkand and Taldykorgan (Figure 1), with a combined population of over 114,000 people.

We describe remote sensing and field observations, and Quaternary dating results, which show that the Lepsy fault has generated at least two substantial earthquakes in the Holocene, the latter of which may have been M_w 8 and is dated to within the last ~400 years B.P. We then characterize the geometry and kinematics of the Lepsy fault, as well as its late Holocene seismic activity, and discuss the role of the fault in accommodating regional N-S shortening related to the ongoing India-Eurasia collision.

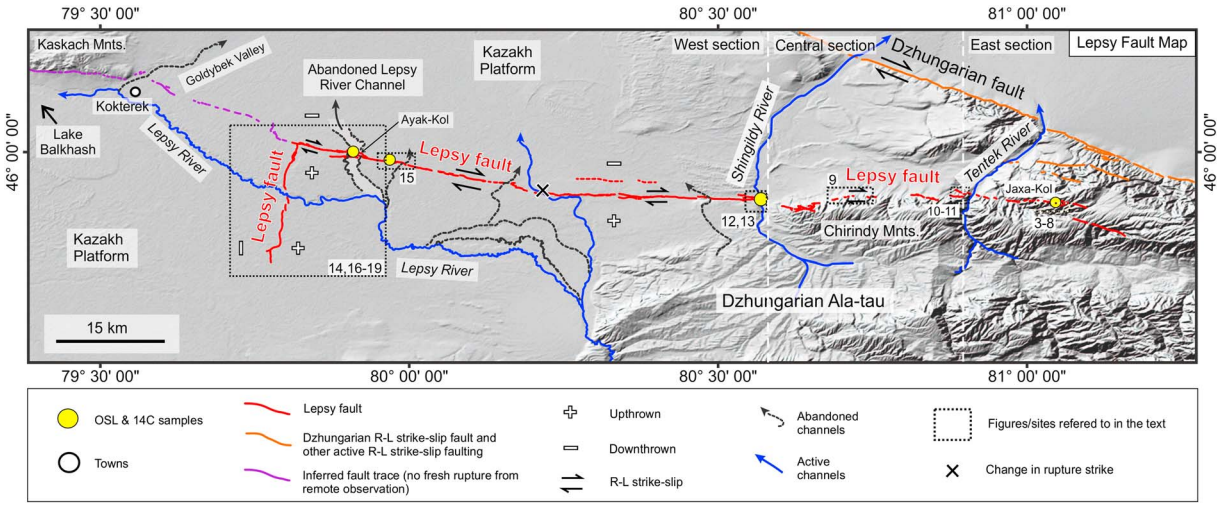

Figure 2. Shaded relief map of the structural and geomorphological features observed along the Lepsy fault from fieldwork and analysis of satellite imagery. The scarp shows both right-lateral and vertical (uplift to the south) components of slip along its entire length. Sites discussed in detail in the text are marked by numbered black dashed boxes. Sample locations are shown by yellow circles. The N-S, dashed white lines delimit the east, central, and west Lepsy fault sections.

2. Lepsy Fault

2.1. Geological Setting

Three types of active faulting dominate the mountains of the northern Tien Shan: NW-SE and NE-SW conjugate strike-slip faults [e.g., *Voitovich*, 1969; *Tapponnier and Molnar*, 1979; *Burtman et al.*, 1996; *Selander et al.*, 2012; *Campbell et al.*, 2013] and E-W oriented reverse faults [e.g., *Avouac et al.*, 1993; *Ghose et al.*, 1997; *Burbank et al.*, 1999; *Thompson et al.*, 2002]. The Lepsy fault scarp (Figure 1), which is the subject of this study, is oriented approximately E-W and extends for ~120 km from the high Chirindy Mountains, a subrange of the Dzhungarian Ala-tau, into the flat, low-lying Kazakh platform, where it terminates abruptly in a N-S oriented fault (Figure 2). An ~10 m high vertical scarp is observed almost continuously in late Quaternary sediments along 120 km of the fault trace in the field. Despite having being originally recognized as potentially active in the Quaternary [*Kurdiukov*, 1956], it is unreported on active fault maps [e.g., *Trifonov*, 1978; *Tapponnier and Molnar*, 1979; *Thomas et al.*, 1996]. The Lepsy fault scarp appears to be on a structure that may continue even further into the platform (see Figure 2 and section 2.5) and into a region where erosion and deposition have removed most of its topographic expression. This westernmost section does not display clear evidence of late Quaternary activity. At its eastern end, the fault is ~10 km SSW from the central section of the Dzhungarian strike-slip fault, a major active NW-SE trending right-lateral fault, over ~300 km long, which bounds the eastern extent of the Dzhungarian Ala-tau [*Voitovich*, 1969; *Tapponnier and Molnar*, 1979; *Campbell et al.*, 2013], and it is likely that the Lepsy fault is a splay from the active Dzhungarian fault. At its westernmost end the Lepsy fault is ~80 km from the NW-SE Aktas fault, whose potential Quaternary activity is unknown (Figure 1).

GPS velocities relative to stable Eurasia indicate that 1–3 mm/yr of N-S shortening must be accommodated north of the Tien Shan (Figure 1) [*Zubovich et al.*, 2010]. Despite low strain rates (10^{-16} s^{-1}) within the platform where the Lepsy fault is sited, the instrumental earthquake record reveals that occasional earthquakes have occurred (Figure 1), but these are all relatively small, with magnitudes ranging from M_w 5.3–6.4 [*Sloan et al.*, 2011]. Well-determined earthquake centroid depths in the Tien Shan forelands and Kazakh platform (Figure 1) indicate that the seismogenic layer is relatively thick (≥35 km) [*Chen and Molnar*, 1977; *Nelson et al.*, 1987; *Sloan et al.*, 2011]. If any of the Palaeozoic structures within the foreland are reactivated in future earthquakes, then the large downdip width of the faults within the platform increases their potential maximum earthquake magnitude.

Figure 2 shows an annotated shaded relief map of the geomorphological features we interpret as fault scarps along the Lepsy fault and which we have mapped from submeter resolution Worldview satellite imagery, additional imagery accessed on Google Earth and Bing Maps, and fieldwork. Figures 3–19 show field observations, which are described in the following sections, beginning in the east and ending in the west. We assess the amount and direction of slip, which are essential in order to establish the fault kinematics and are useful in the

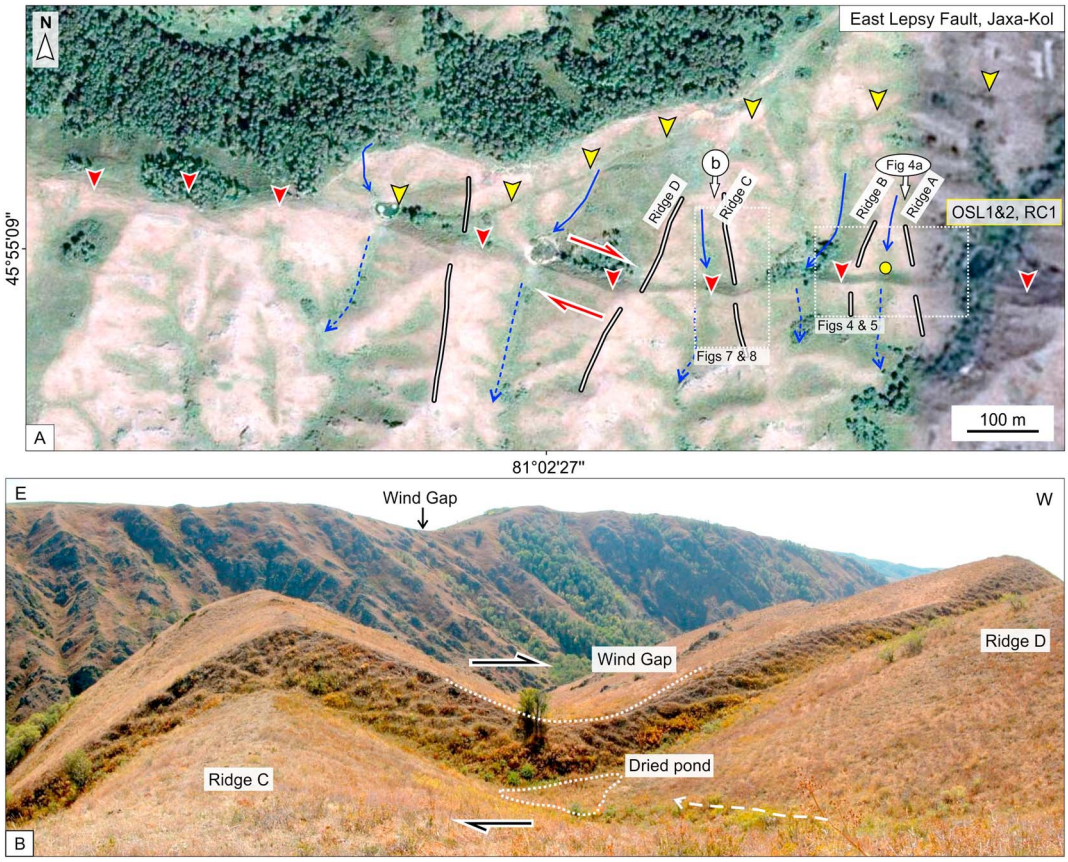

Figure 3. East Lepsy fault map and the Jaxa-Kol field site. (a) Google Earth (source for all Google Earth images: earth.google.co.uk/) image showing the main E-W scarp (red triangles) and a secondary scarp (yellow triangles) that splays to the NE crossing N-S oriented ridges in the high Chirindy mountains of the Dzhungarian Ala-tau, SE Kazakhstan. The scarp uplifts the south side relative to the north side and right laterally offsets a series of channels (solid and dashed blue arrows) and ridge crests (solid black-white lines). Wind gaps are preserved on the south side, and a series of (mostly dried) ponds have formed against the scarp. The location of the field photo in Figure 3b is marked (black arrow), and the sampling site is shown (yellow circle); (b) View south of ridges C and D showing ~10 m vertical offset and significant right-lateral offset.

assessment of earthquake hazard. The following sections present our observations. We discuss the fault kinematics in section 3.1. The details of our methods for estimating vertical and horizontal displacements, and all Quaternary dating procedures, are described in appendices.

2.2. East: Jaxa-Kol Section

2.2.1. Overview

In the east, the fault scarp crosses N-S trending ridges in high (~1450 m elevation) mountain topography of the Dzhungarian Ala-tau (Figures 2 and 3). A regionally extensive south tilted peneplain surface separating Paleozoic and overlying Cenozoic rocks [*Chediya*, 1986; *Mikolaichuk et al.*, 2003; *Cunningham et al.*, 2003] is preserved throughout the Dzhungarian Ala-tau. Abandoned drainage channels within the peneplain surface south of the Lepsy fault, which are preserved as what we interpret to be wind gaps, attest to cumulative fault movement of ≥100 m (Figure 3).

The main scarp strikes E-W and follows a bedding plane in resistant Paleozoic bedrock, which dips steeply north (80°N) and is covered by a thin veneer of soil stabilized with thick vegetation (Figure 3b). Vertical and right-lateral displacement of a series of ridge crests and adjacent channels has resulted in ponding of drainage against the upthrown southern side (Figures 3–5) and smaller-scale ponding of channel thalwegs against reactivated distributed bedding planes with offsets of typically tens of centimeters. Although the main scarp is concentrated on a single bedding plane, a secondary scarp extends northeast of the main scarp trace for 1.5 km (Figure 3). Analysis of satellite imagery indicates that the main fault scarp continues eastward for a further 4 km from the view shown in Figure 3 to ~81°05′E with a more southeasterly strike of ~110°

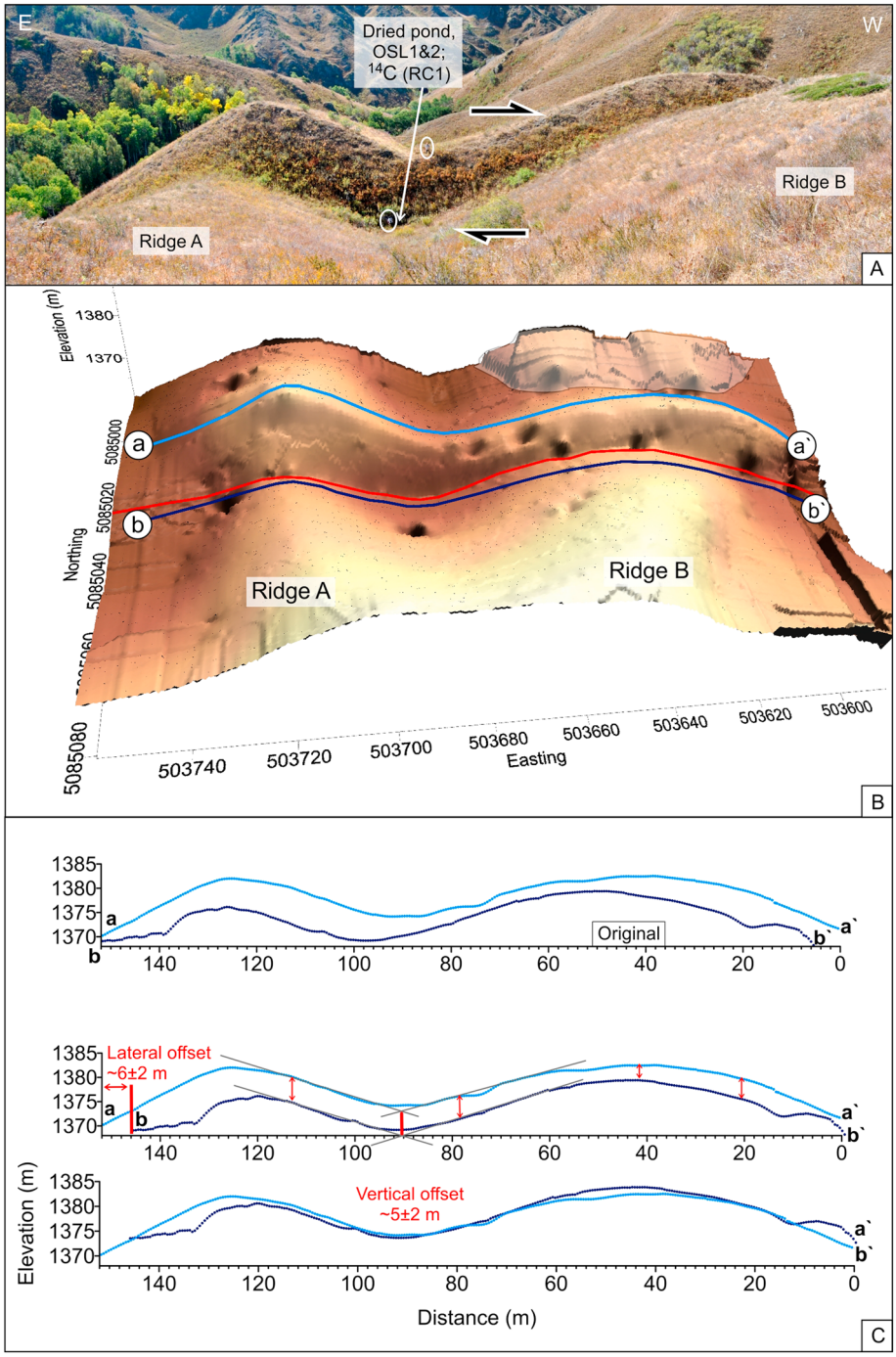

Figure 4. (a) View south of ridges A and B (see Figure 3 for regional location). The south side is uplifted relative to the north side. Right-lateral displacement is revealed by the asymmetry of the offset ridges across the fault. People for scale (white circles) stand in the channel thalweg on the north side where there is a dried pond and on the (upthrown) south side where there is now a wind gap. (b) Digital elevation model (DEM) of ridges A and B generated from gridded Differential Global Positioning System (DGPS) points from a field survey (individual survey points have horizontal and vertical uncertainties of ~10 cm, and the DEM is gridded at a 50 cm pixel spacing). The DEM shows the traces of fault-parallel elevation profiles *a*-*a*′ (light blue) and *b*-*b*′ (dark blue) on the hanging wall and footwall, respectively. (c) Fault-parallel elevation profiles generated from the DEM shown in Figure 4b, also shown in Figure 5. Restoration of ~6 m right-lateral slip realigns the well-defined channel thalweg (the center point of which is defined by the vertical red line between ridges A and B) on either side of the fault. Around 5 m of vertical offset then totally realigns the topography on either side of the fault to form a single continuous "prefaulted" surface. Note that the vertical offset required to align the topography underestimates the vertical displacement across the scarp, as it does not account for the southward topographic slope.

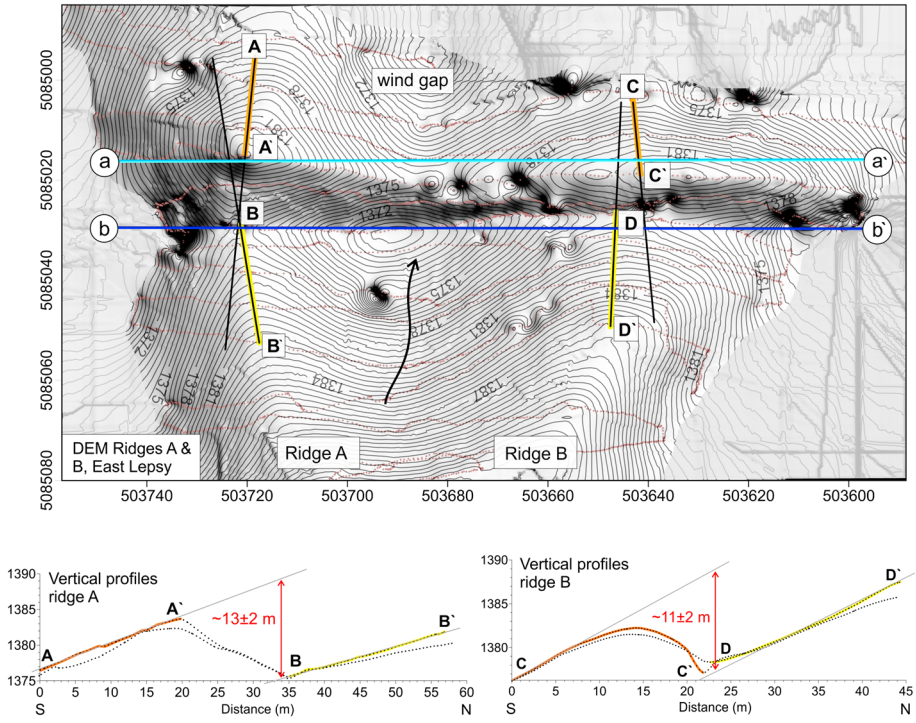

Figure 5. Offset ridges, east Lepsy fault. (top) Digital elevation model (DEM) of ridges A and B generated from gridded Differential Global Positioning System (DGPS) points. The *x*, *y*, *z* points from which the DEM was constructed are shown as brown dots. Each survey point has uncertainties in horizontal and vertical locations of ~10 cm. The black arrow shows the direction of streamflow to the south, which is ponded against the fault scarp. A wind gap is preserved on the south side of the fault. To estimate the vertical displacement across the scarp, we are restricted to making measurements across the offset ridge crests, as the gradient of channel bottoms has been altered by erosion and deposition, and the large lateral component makes matching the sloping hillsides difficult. The tracks of the vertical (orange and yellow lines) and lateral (light and dark blue lines) fault elevation profiles are shown on either side of the fault. The vertical profiles are shown in Figure 5 (bottom). The lateral profiles are shown in Figure 4c. (bottom) Profiles along the crests of ridges A and B show similar gradients on both sides of the fault and yield estimates of ~13 ± 2 m and ~11 ± 2 m vertical offset, respectively.

(see Figure 2). At its easternmost extent, the scarp bends southeastward and terminates in a series of smaller secondary splays.

2.2.2. Geomorphology

We generated digital elevation models (DEMs) of three adjacent shutter ridges (labeled A, B, and C, from east to west along strike, shown in Figure 3) using gridded Differential Global Positioning System (DGPS) measurements (Figures 4, 5, and 8). Uncertainties in horizontal positions and heights of the individual survey points are less than 10–20 cm and are negligible compared with small-scale relief on the ridge surfaces surveyed at this site and alluvial surfaces surveyed at later sites. To generate a DEM, a regular grid was constructed from the irregularly spaced *x*, *y*, *z* points. The pixel spacing in the DEM is 0.5 m.

Between ridges A and B (Figures 4 and 5), a well-defined channel thalweg indicates ~6 ± 2 m of right-lateral slip. Topographic profiles along ridge crests A and B show a vertical offset of 13 ± 2 m and 11 ± 2 m, respectively (Figure 5). There is some ambiguity in trying to determine the fault dip direction and hence the nature of fault motion at this site, because the fault follows bedding that dips very steeply, 80°N, and is unlikely to represent the fault dip at depth. We also observe distributed bedding plane slip manifest as decimeter vertical offsets (south side down), on a series of almost vertical beds, over a distance of ~100 m to the south of the main scarp (e.g., Figure 6). Ridge C (Figures 3, 7, and 8) is 160 m west of ridges A and B and records 4 ± 2 m of right-lateral slip and ~9 m of vertical slip (Figure 8), considerably less than the measurements from A and B, but with a similar ratio of vertical and horizontal displacements.

2.2.3. Scarp Age

At this eastern site, three samples (OSL1, OSL2, and RC1; Tables 1 and 2) were collected from an ~1.20 m deep pit in dried pond sediments, which have accumulated between ridges A and B after scarp formation, and

Figure 6. View SW from ridge B of steeply north dipping Paleozoic bedding planes (white arrows). The Lepsy fault trace is marked with red triangles with people for scale (white circles) standing on ridge A. Black dashed lines show potential vertical offsets on consecutive bedding planes over a distance of ~100 m to the south of the ~10 m scarp.

blocking of a small south flowing channel (Figure 5). The pit stratigraphy revealed ~30 cm of stony dark top soil, which graded into a homogeneous silt unit. This silt was underlain by interbedded medium sand-gravel and homogeneous silt layers and a dark organic-rich soil with angular ~1 cm bedrock fragments. We infer that the sand and silt units represent ponding against the scarp and were therefore deposited after some amount of offset on the fault. The dark soil beneath these former units might represent the original prefaulted surface or alternatively a dry period during which a soil layer formed on top of older pond units formed against a preexisting scarp.

OSL1 was collected from silt unit at a depth of 0.85 m and yielded an age of 1770 ± 510 years B.P. providing a minimum age estimate for scarp formation. OSL2 was taken from silt unit B at a depth of 0.65 m and yielded an age of 910 ± 520 years B.P. and also provides a minimum age estimate for scarp formation. A single

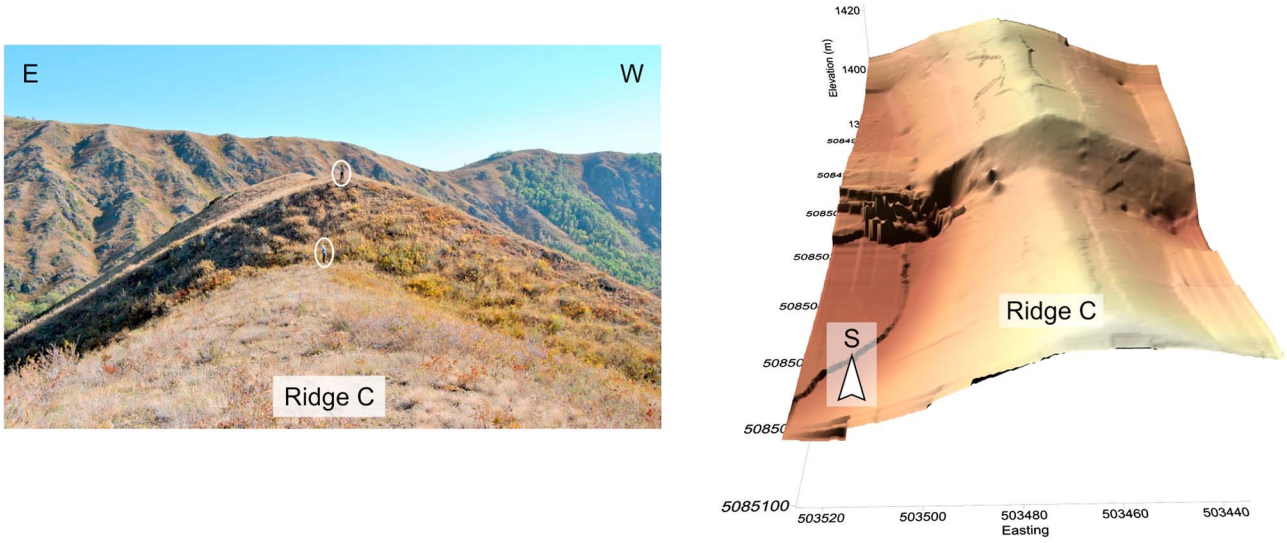

Figure 7. View south of offset ridge C with people standing on the ridge crest either side of the fault (white circles) for scale. A DEM generated from field DGPS survey of the same area. See Figure 8 for the elevation profiles measuring fault vertical and lateral offsets.

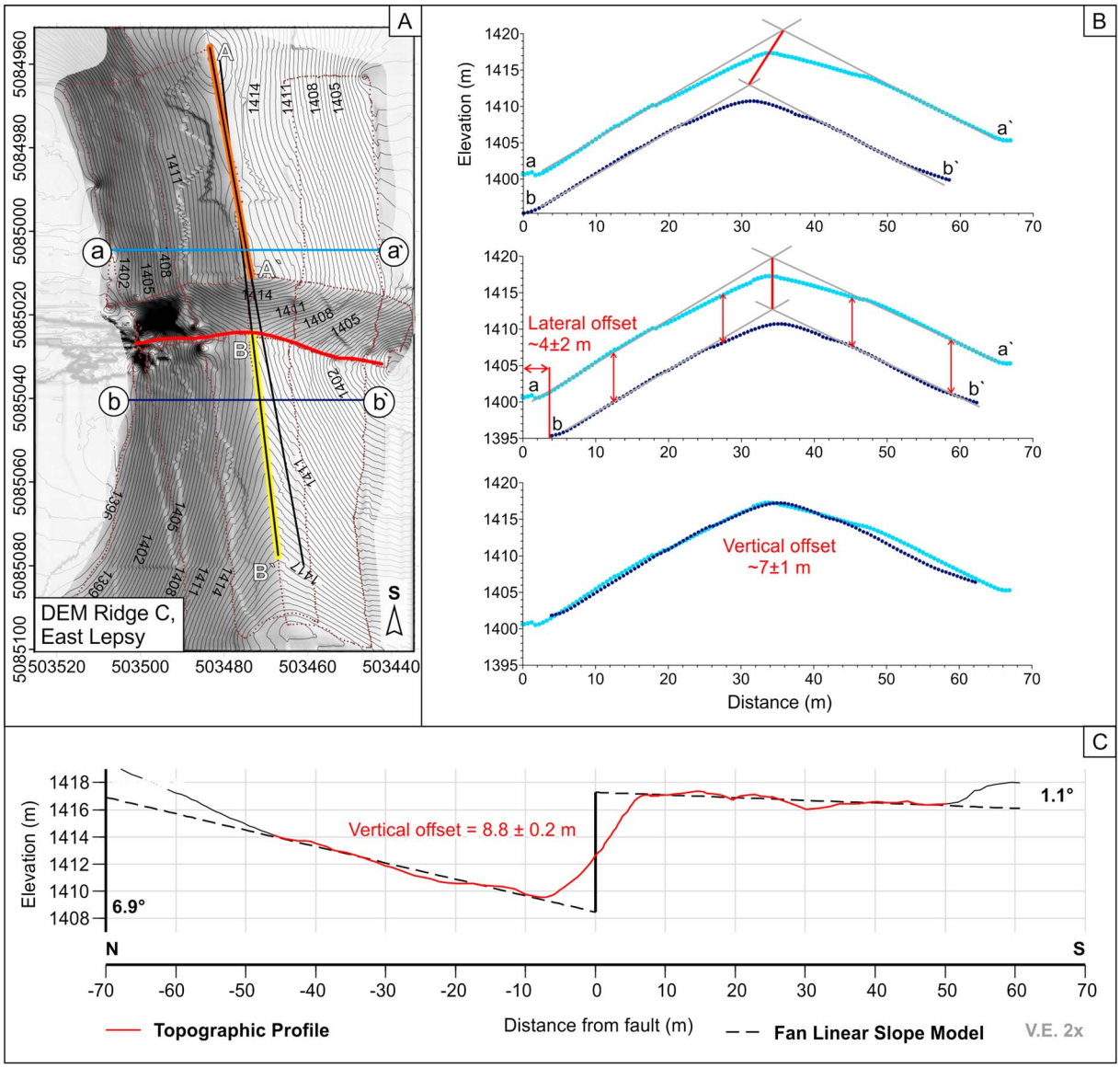

Figure 8. (a) Field DGPS-generated DEM of ridge C. The x, y, z points from which the DEM was constructed are shown as brown dots. Each survey point has uncertainties in horizontal and vertical locations of ~10 cm. (b) Fault-parallel elevation profiles on either side of the fault record 4 ± 2 m of right-lateral offset. Approximately 7 m vertical slip restores the total amount of offset and restores the topography back to an original prefaulted surface. Note that the vertical offset required to align the topography underestimates the vertical displacement across the scarp, as it does not account for the southward topographic slope. (c) A fault-perpendicular elevation profile along the ridge crest shows different slopes on either side of the fault, introducing additional uncertainty in estimating the vertical displacement. We assign an uncertainty of ±2 m to the 8.8 m displacement measured across the center point of the scarp, which reflects variability in displacement depending on whether it is measured at the base or at the top of the scarp; see Appendix A for more details.

bulk radiocarbon sample (RC1) collected from the dark, organic-rich soil at a depth of 1.05 m gave an age of between 1988 and 1806 calibrated radiocarbon years B.P. The increase in age with depth is consistent with stratigraphic position. We interpret the basal dark soil beneath the interbedded gravel-sand-silt units as representing periods of downslope transport of gravel followed by settling of fines in a pond. Because we cannot be sure that the dark soil is the true base of the pond, these dates allow us to infer that the scarp has been present in this location, at least in some form, since at least ~2000 years ago.

2.3. Central Section: West of the Tentek River

2.3.1. Overview

Between the north flowing Tentek and Shingildy Rivers, (80°54′E and 80°34′E, respectively) the Lepsy scarp continues for 25 km along the Chirindy range front, with peak heights ~800–900 m above the range front (Figure 2). Several parallel lines of surface rupturing are observed, defining a fault zone up to 1 km wide, and

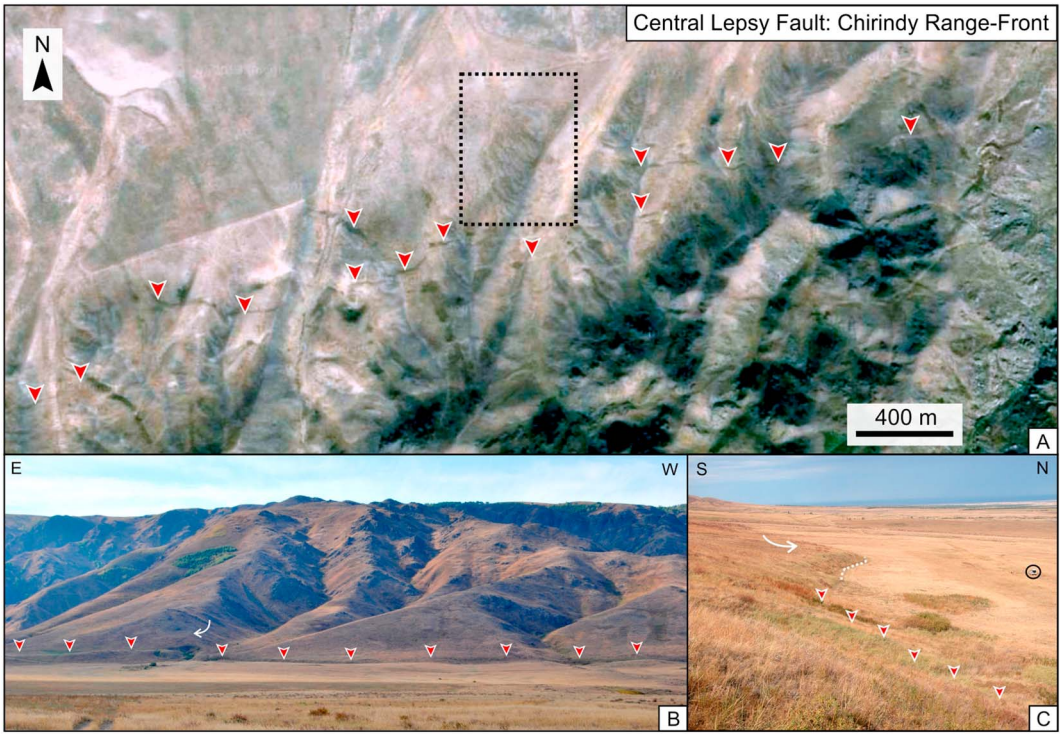

Figure 9. The central Lepsy fault. (a) Google Earth satellite image centered at 45°55′N/80°41′E shows a characteristic section of the central Lepsy fault where it bounds the lower relief of the Chirindy range front (see Figure 2 for the regional figure location). A 1 km wide zone of distributed deformation is marked out by several subparallel lines of surface rupturing (red triangles). The black dashed box shows the lobate morphology and wrinkle ridge surface texture, which is characteristic of landslide deposits (in alluvium and loess). (b) View south from 45°56′N/80°51′E, showing continuous ~10 m vertical offset preserved in Quaternary alluvium (red triangles) also characteristic of the central Lepsy fault. A small scallop landslide in the fault scarp is shown (white arrow shows the direction of motion in landsliding). (c) View west of landsliding in loess (the white solid arrow shows the direction of sliding, and the white dashed line marks the landslide toe), also characteristic of the central fault section. Vehicle circled for scale.

slumping in thick loess cover is pervasive (Figure 9). In places, two parallel scarps are visible in satellite imagery (Figure 10a). The Chirindy range ends east of the Shingildy River, but the late Quaternary fault scarp continues westward through the steppe (Figure 12). Cenozoic red beds exposed south of the fault scarp, in cuttings of the Shingildy River, are folded into a gentle anticline over a wavelength of ~2 km and contain minor south dipping reverse faults (Figure 13). We observe a fault dip of ~50°S preserved in poorly exposed bedrock in a smaller river gorge west of the Tentek River at 45°55.706′N/80°53.847′E (Figure 10c).

2.3.2. Geomorphology

Although more discontinuous in this central section relative to the eastern part, the main scarp trace still uplifts the south side (range front) relative to the north side (foreland) as a 5–10 m vertical offset in Quaternary material (Figure 10). At 45°55′N/80°52′E, where there is no evidence of slumping in the loess cover, the main scarp is preserved as a vertical offset in an alluvial fan surface (Figure 10). The local strike at this site is ~110°. The estimated vertical displacement varies between ~6 m and ~9 m within the four individual topographic profiles shown in Figure 10d. The variation may arise from the locally steeper slopes found on the southern, upthrown, side of the scarp, where the alluvium grades into steeper hillslope colluvial deposits. Given that the profile showing the largest scarp height of ~9 m also shows steep slopes on its southern side, we exclude it and estimate the likely full range of vertical displacement at this site to be 5–8 m. A well-preserved N-S oriented fluvial riser also records 7 ± 2 m of right-lateral offset at this same location (Figure 11). We did not collect samples for dating from this site, but the scarp here is preserved in alluvium, as opposed to the resistant bedrock in which it is preserved in the east at Jaxa-Kol; therefore, we suggest that the scarp here is at least comparable in age to the scarp at Jaxa-Kol, if not younger. We also note that postuplift stream incision has only migrated upstream by ~50 m, where a prominent knickpoint is visible (Figures 11a and 11b). There is no evidence of older offsets, in the form of higher river terraces, recorded in the geomorphology south of

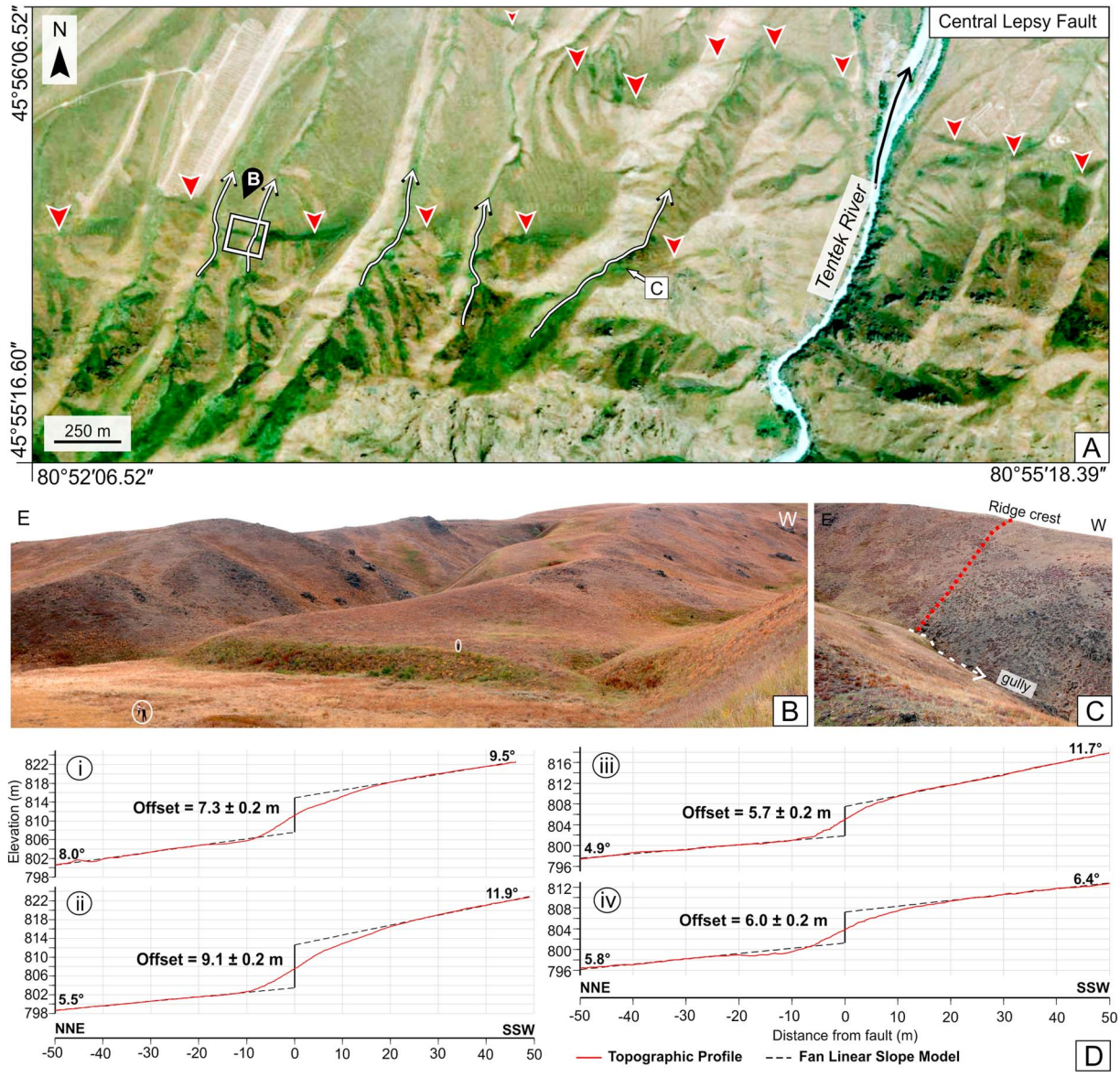

Figure 10. (a) Google Earth satellite image showing an overview of the Tentek River field site. The Lepsy fault is observed as two north and south subparallel strands (red triangles). The white box shows the area of the DEM in Figure 11b. The location of field photos are shown: (b) view SSW of the main Lepsy scarp preserved in late Quaternary fan material with people circled for scale and (c) view SW from 45°55.706′N/80°53.847′E, showing the fault dip of ~50°S preserved in bedrock in a gorge west of the Tentek River gorge. The slopes are vegetated, obscuring the view of the fault in the photograph. However, the fault can be inferred from a subtle color change (arising from a juxtaposition of two bedrock types) between the north side and south side of the fault (marked by the red dotted line) and a height change at the ridge crest. (d) Scarp elevation profiles i–iv, derived from a series of NNE-SSW profile lines from the DGPS DEM shown in Figure 11b and numbered in order from east to west. Profiles show variable vertical offset that we interpret to arise from the presence of steeper colluvial deposits on the upthrown side. We estimate that the actual scarp height is within the range ~5–8 m.

the fault. At the western end of the central section, at the Shingildy River (Figure 12), we measured a scarp height of 7.4 ± 1 m using DGPS.

2.3.3. Scarp Age

At the Shingildy River, we collected samples OSL3, OSL4, and RC2 (Tables 1 and 2, respectively) from the 7.4 ± 1 m high scarp where it is preserved in a terrace on the west side of the Shingildy River (Figure 12). OSL3 was collected from the base of the Loess cap, 5 cm above the contact with the river gravels (Figure 12b), at a depth of 1.05 m below the surface, or ~6.5 m above the river bed. OSL3 consisted mainly of fine silt, with some evidence of fluvial reworking in the form of fine- to medium-grained sand interbedded on a 5 cm scale and yielded an age of 2190 ± 470 years B.P. OSL3 provides a postdate on the major period of fluvial gravel deposition that formed the terrace. OSL4 was collected from a medium-grain sand unit within coarser river

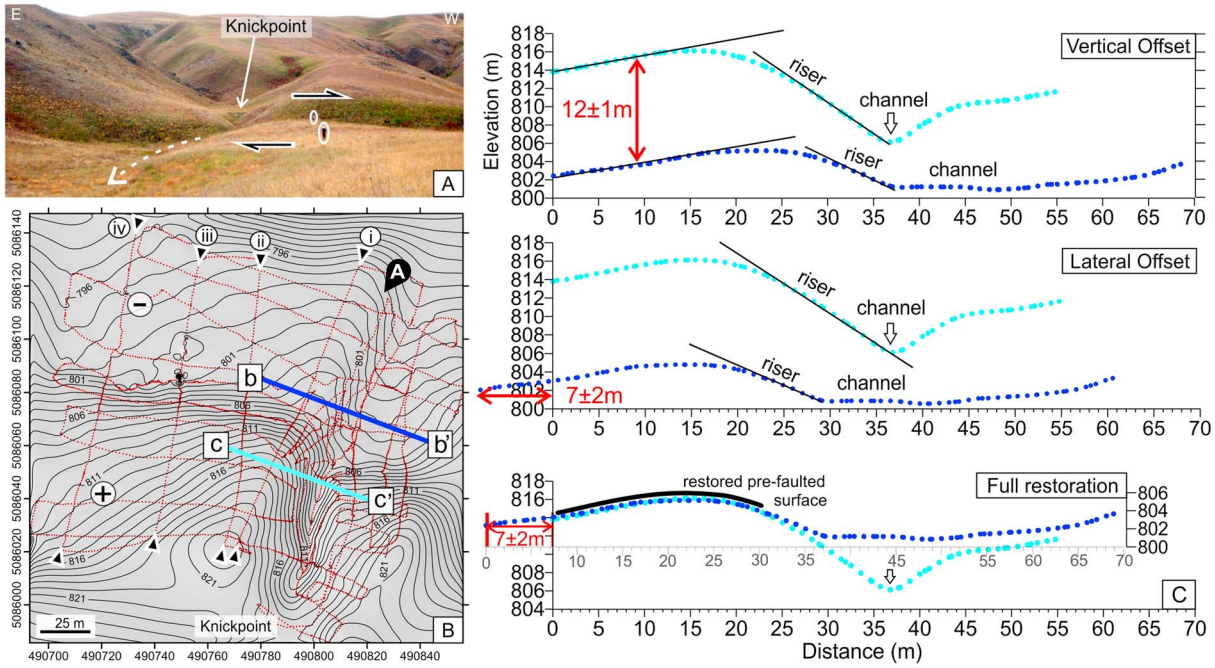

Figure 11. (a) View south of a right laterally displaced fluvial riser (people for scale) from the location shown in Figure 11b. (b) DGPS-derived DEM of the Lepsy fault scarp at the site area marked in Figure 10a. See the main text for DEM resolution and details of offset and error measurements. The DGPS survey track is shown in brown dots, scarp-perpendicular elevation profiles i–iv are marked by labeled black triangles and are shown in Figure 10c. The fault strike at this site is ~110°. Note that a knickpoint has only migrated ~50 m into the uplifted fault hanging wall. (c) Scarp-parallel elevation profiles showing the original (top), lateral (middle), and total (bottom) offsets across the Lepsy fault. The thick black line (Figure 11c, bottom) represents the original, prefaulted surface after the total slip is restored.

gravel at ~0.50 m below the base of the loess cap and yielded an age of 5010 ± 700 years B.P., which is consistent with its lower stratigraphic position. A radiocarbon sample of charred gravel (RC2) was collected ~0.40 m lower in the stratigraphy than OSL3, but at the same sampling site, from a burned layer preserved in the river gravels (Figures 12b and 12d). However, the ^{14}C concentration in this sample was not high enough to yield a radiocarbon age. The available age constraint suggests that this terrace was uplifted at least ~5000 years B.P., which is consistent with the minimum age estimates of scarp formation dated by both radiocarbon and OSL dating methods in the east at Jaxa-Kol (~2000 years B.P.; section 2.2).

We have no direct age constraints on the scarp at the Tentek River site (Figures 10 and 11), though there are suggestions that it is relatively young and also that it is potentially formed in a single event. The scarp crosses several stream beds, one of which is shown in Figure 11. Although the scarp has uplifted the upstream parts of the channels, their beds are relatively intact, with narrow incisions that have migrated only ~50 m upstream.

2.4. West: Ayak-Kol

2.4.1. Overview

The Chirindy Mountains end at the Shingildy River (Figure 2). West of this point there is no sharp relief other than the vertical offset preserved along the Lepsy fault in sand dunes and loess cover. Between the Shingildy River and ~80°13′E the fault strikes E-W for ~25 km, where the fault changes strike to ~110° (black cross in Figure 2) and continues for a further 30 km. This ~55 km long western fault section is characterized by a single 9–10 m vertical step, with the south side uplifted relative to the north.

Ayak-Kol, near the western end of the fault scarp at (45°59.931′N/79°54.901′E, Figures 2 and 14a), is a small (~120 m^2) lake formed by a spring on the fault. At Ayak-Kol the 9–10 m high scarp splits into two parallel scarps with different amounts of vertical offset, a northern one with height 5.6 ± 1.5 m and a southern one ~2 m high (Figure 14a). Several north flowing river channels are abandoned (Figure 2 dashed black arrows) and/or diverted westward, including the Lepsy River itself. Although these river diversions may simply be due to channel switching, rather than being caused by an earthquake, the age of the fluvial sediments places a valuable constraint on the maximum age of the most recent event, as we discuss below. At ~79°50′E the

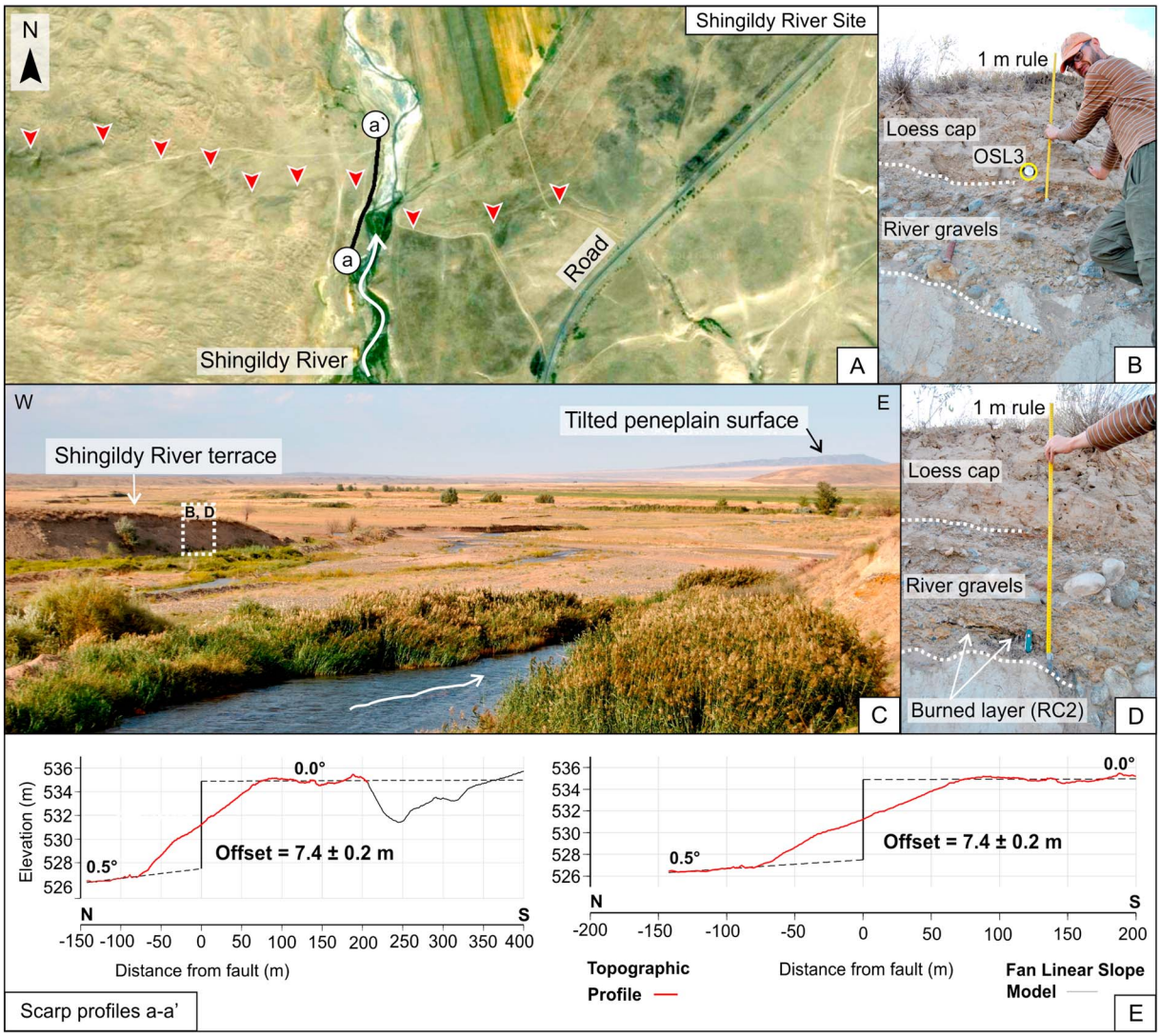

Figure 12. The Shingildy River site (a) Google Earth satellite image, centered at 45°54′/80°34′, showing an overview of the Shingildy River site. The Lepsy fault scarp is marked by red triangles, and the trace of the DGPS west river terrace elevation profile track *a*-*a*′ is shown; see Figure 12e for scarp offset measurements. (b) View west of the sample OSL3, taken from the base of the loess cap terrace river gravel contact. (c) View NW showing the north flowing Shingildy River and west terrace sampling site (dashed white box). The south tilted peneplain is also shown in the far distance. (d) View west of a burned layer containing charred gravel (RC2, Table 2) taken at ~0.50 m depth within the river terrace gravels. (e) N-S scarp profile *a*-*a*′ showing 7.4 ± 1 m (total measurement error; see Appendix A) offset preserved in the late Quaternary river terrace. The left-hand panel shows the full topographic profile, whereas the right-hand panel shows a closer view of the terrace adjacent to the fault scarp.

5.6 ± 1.5 m high E-W scarp changes strike by 90° to trend N-S. The scarp height decays southward over a distance of ~22 km (Figures 2 and 14b).

2.4.2. Geomorphology

Along the 55 km length of the Lepsy fault in the platform, a 9–10 m of vertical offset (e.g., Figure 15) is preserved in the sand dunes and loess cover. Left-stepping, en echelon pull-apart basins are also preserved along strike of the main scarp, with basin dimensions ranging between 0.3 to 3 km length (Figure 15). The en echelon arrangement of surface faulting has generated these basins and is consistent with right-lateral faulting.

At Ayak-Kol 45°59′N/79°46′E, the single 9–10 m scarp splits into two parallel segments, which have heights of 5.6 ± 1.5 m (northern branch) and 2 ± 1 m (southern branch). Both scarps have a south side up sense of vertical motion. The southern branch of the scarp is left stepping and segmented and can be traced westward for 3.6 km to 45°59′N/79°52′E where it ends (Figure 14), whereas the 5.6±1.5 m high scarp continues a further 4 km and terminates along a N-S fault, which we discuss in section 3.2. The southern, ~2 m high, scarp crosses

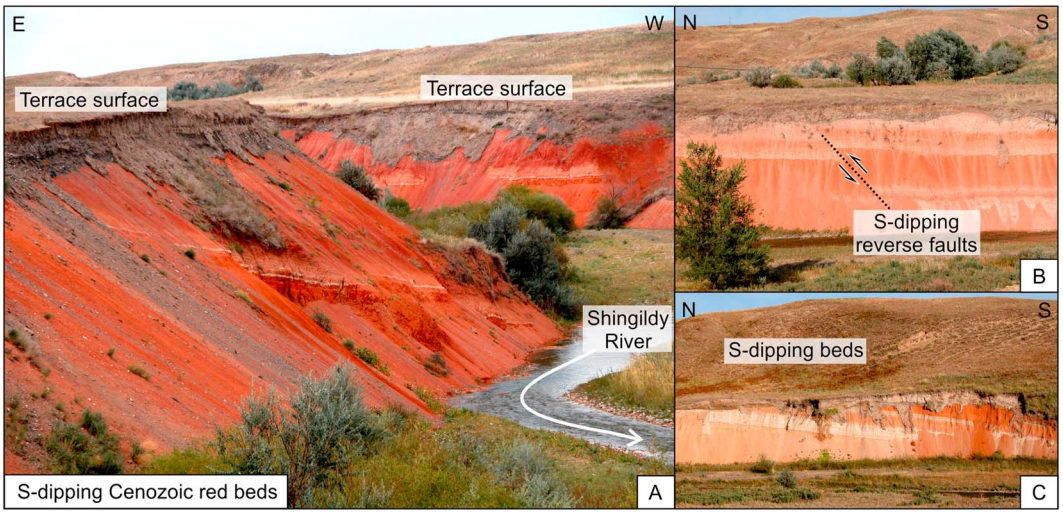

Figure 13. South dipping red beds at the Shingildy River site. (a) View south of south dipping Cenozoic red beds and the well-preserved terrace surface. (b) View east of minor reverse faulting in Cenozoic red beds. (c) View east to south tilted Cenozoic red beds. All photos taken from a 2 km walk south along the Shingildy River.

the abandoned channel of the Lepsy River (Figures 14 and 19) but is not preserved in the bed of the channel itself. Fault-parallel elevation profiles across the abandoned channel indicate that it is more deeply incised on the south side of the ~2 m scarp than on the north side (Figure 19c), indicating that the river was able to continue flowing after this 2 m step-forming event. This southern scarp, which the river has been able to erode into and retain its course, hence formed in an earlier event (or events) than the main 5.6 ± 1.5 m high scarp, which is not eroded even within the old river bed.

2.4.3. Main Scarp Age

We collected an OSL sample and two radiocarbon samples (OSL5, RC3, and RC4; Tables 1 and 2) from an ~1.40 m deep soil pit excavated into a small pull-apart basin at (45°59′N/79°57′E, Figures 2 and 15) along the main 9–10 m scarp. The pit stratigraphy revealed 10 cm of black top soil, underlain by fine beige sands and clay until ~0.60 m depth, where there was an ~5 cm thick dark soil. Beneath this soil unit, dark silt-clay continued to the base of the pit, which was waterlogged. RC3 was a bulk radiocarbon sample taken from the 5 cm thick soil unit at a depth of 0.55 m from which charcoal of a gymnosperm small branch yielded a radiocarbon age of 558 to 380 calibrated radiocarbon years B.P. OSL5 was taken from a pale beige fine sand unit directly below the dark soil at 0.60 m and yielded an age 300 ± 150 years B.P. An additional OSL sample was collected from the dark silt-clay material at the base of the pit at a depth of 1.30 m. However, this sample did not yield an OSL signal and is not reported in Table 1. Bulk sample RC4 was taken from 1.30 m depth from dark grey clay, but this sample yielded a date indistinguishable from modern. Although we have no constraint on the depth of the base of the pond, samples RC3 and OSL5 indicate that the Lepsy scarp was present in some form here since at least ~300 to 500 years B.P.

Further west at 45°59′N/79°54′E (Figures 14 and 16), where the fault consists of two parallel strands, a quarry exposure excavated through the northern, 5.6 ± 1.5 m high, scarp revealed a fluvial sequence of well-sorted cross-bedded sands, capped with 40 cm of wind-blown loess. Two samples from a sedge bed (Figures 17b and 17c) preserved within this fluvial sequence, which include Cyperaceae leaves (sedges) covered with a mineral coating, and a fragment of pine bark, yielded radiocarbon ages of 375 to modern and 348–66 calibrated radiocarbon years B.P., respectively (samples RC5 and RC7, Table 2). A small fragment of plant resin (RC6) from ~5 cm below the sedge bed yielded an age >57,800 years B.P. The hard nature of the resin material and its much greater age indicates that this sample has residual age and we do not consider it further. A single OSL sample of the fine quartz sand from 5 cm below the sedge deposit gave an age of 430 ± 120 years B.P. (OSL6, Table 1). These ages and their context are very significant as the sedges are overlain by fluvial channel deposits, indicating that the river was still flowing northward <400 years ago (Figure 18).

If the main scarp formed at any measurable time prior to abandonment of the stream, it would have been incised into by the river, but this is not the case. The scarp must, therefore, have formed during or after stream

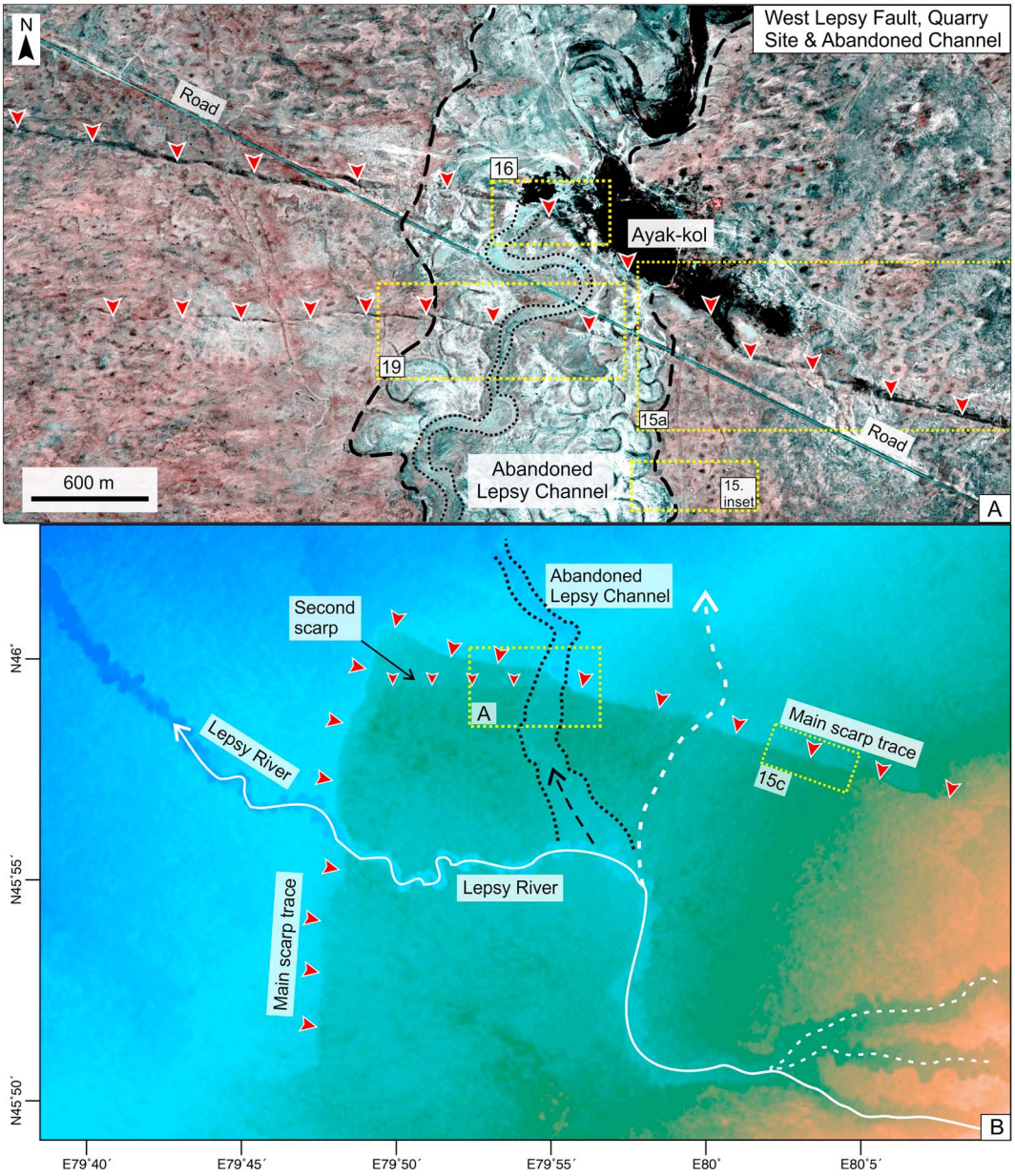

Figure 14. West Lepsy fault termination. (a) Worldview satellite image of the main Lepsy fault trace (5.6 ± 1.5 m vertical offset) at Ayak-Kol. The yellow dashed boxes show the locations of Figures 15, 16, and 19. The main scarp crosses the abandoned N-S oriented Lepsy River flood plain (bright white pixels and black dashed boundary). The most recent active channel within the flood plain is also shown (dotted in black). We infer that the N-S river course was abandoned after the 5.6 ± 1.5 m offset event (see section 2.2). Ayak-Kol has formed against the uplifted south side of the Lepsy fault. A secondary subparallel segmented, left-stepping scarp is also preserved to the south of the 5.6 ± 1.5 m fault scarp. (b) The 90 m resolution Shuttle Radar Topography Mission (SRTM) DEM of the western fault termination. The yellow dashed box denotes the area shown in Figure 14a. The Lepsy River now flows westward (solid white arrow); the abandoned northward river course is also seen clearly (black dashed arrow). Possible older drainage deflections are also noted (white dashed arrows), which may relate to older events. It is possible that such older events only generated enough vertical offset to partially divert the flow of the Lepsy River.

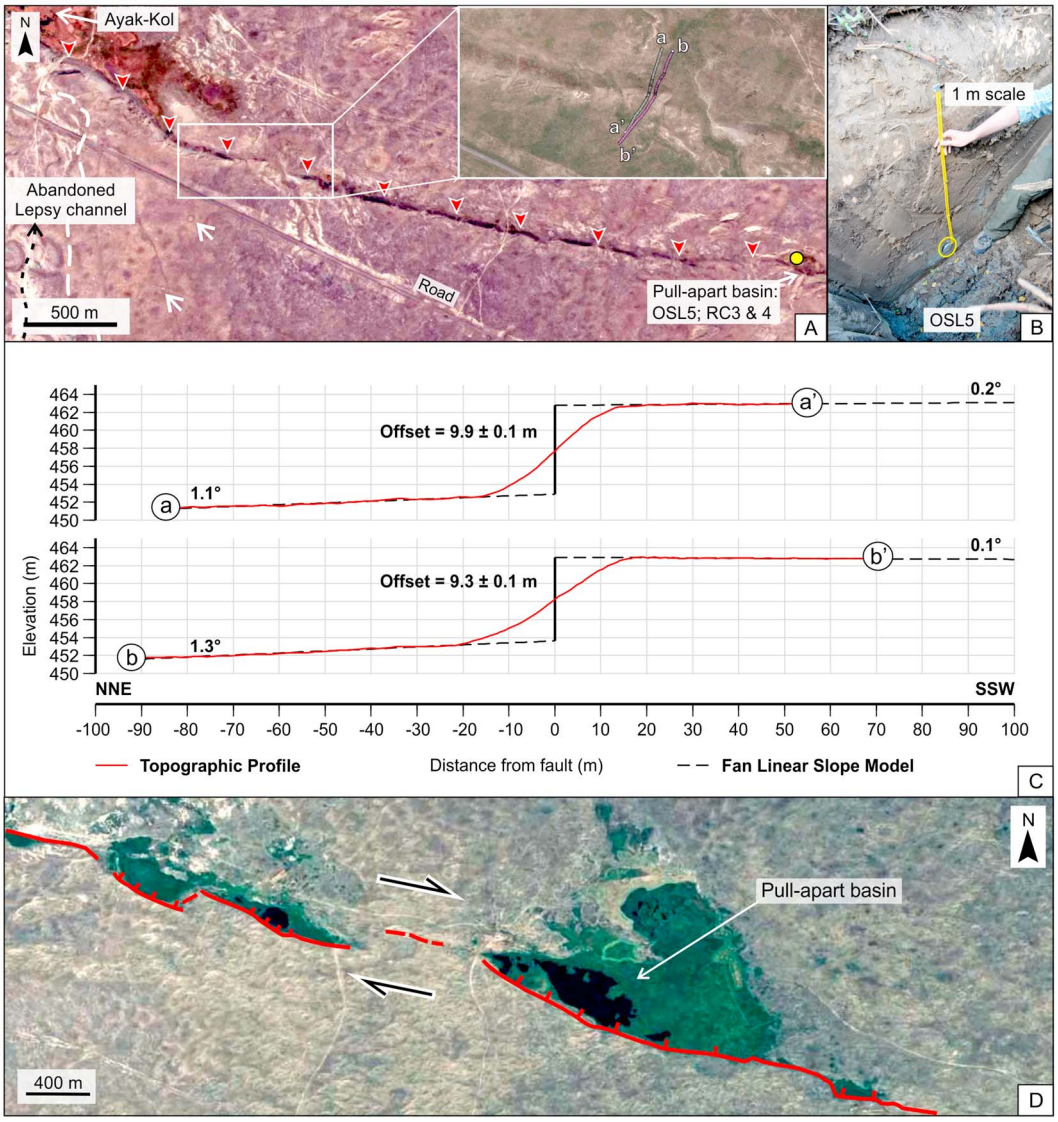

Figure 15. West Lepsy fault, main scarp; no other relief is observed in this part of the Kazakh platform except the ~10 m vertical fault offset. (a) Worldview satellite image showing the main Lepsy scarp (red triangles) and location of a small pull-apart basin, which is also the location of samples OSL5 and OSL6 (yellow circle and Table 1) and RC3 and RC4 (Table 2). The small white arrows point to grave circles that appear to be sited along the east bank of the abandoned Lepsy River channel. The inset shows two scarp-perpendicular DGPS profiles, offsets shown in Figure 15c. (b) The pull-apart basin sample pit stratigraphy and the location of sample OSL5 (see section 2.4 for details). (c) DGPS scarp elevation profiles, see Figure 15a for profile locations, record 9–10 m of vertical offset of a very gently dipping surface and with uplift of the south side relative to the north side. (d) Google Earth satellite image centered at 45°57′N/80°04′E, showing left-stepping, en echelon pull-apart basins, which are consistent with right-lateral slip.

abandonment—hence in the last 400 years. Given the young age of the uplifted fluvial sands, we find it most plausible that the 5.6 ± 1.5 m scarp preserved in the river bed formed in a single large-magnitude event, rather than forming in multiple earthquakes, for which there is no evidence in the documented historical record [*Mushketov*, 1785]. Additionally, given the very low relief of the Kazakh platform, it is possible that this amount of offset prompted the switching of the Lepsy River. We discuss this possibility more in section 3.2. A row of grave mounds (Kurgans; typical structures of the Bronze Age in central Asia) is also aligned along the abandoned channel (Figure 15a; white arrows), suggesting that water was still flowing northward until at least ~2–3 ka [*Sala and Deom*, 2005].

Two further radiocarbon samples (RC8 and RC9, Table 2) were collected from deeper in the fluvial stratigraphy at the same quarry site, where a sand boil has deformed the overlying channel deposits (Figure 17d),

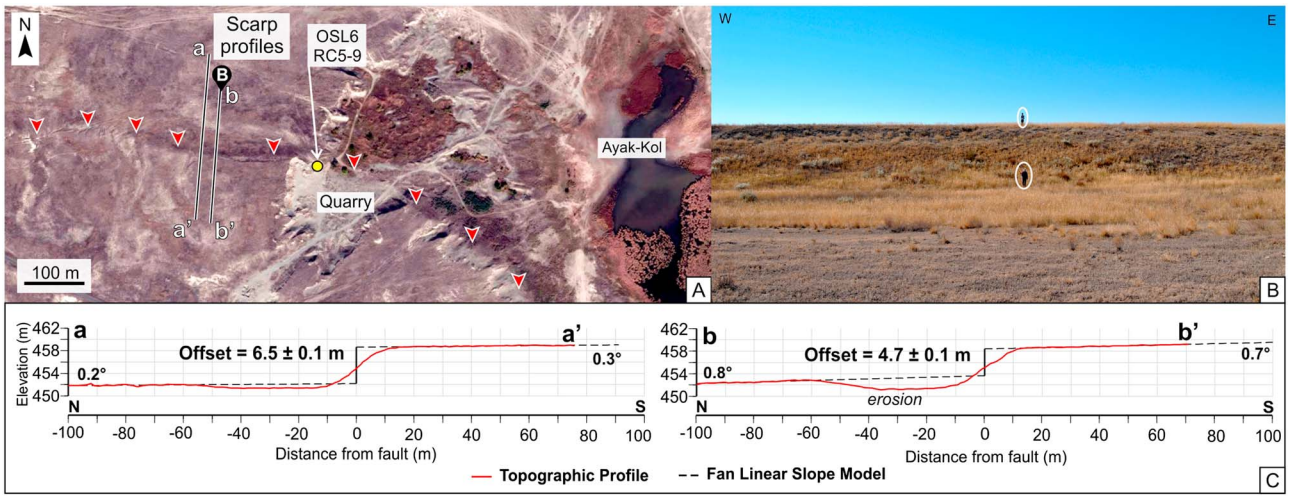

Figure 16. West Lepsy fault quarry site and Ayak-Kol. (a) Worldview satellite image centered on 45°59.972′N/79°54.437′E of a quarry excavation through the main Lepsy scarp (red triangles), showing sample locations (yellow circle), DGPS scarp profiles (black-white lines), and the location of field photo in Figure 16b. (b) View south of the main scarp (people for scale), which has a south side up sense of motion. (c) Two DGPS scarp elevation profiles show variable scarp heights of ~4.7 m and ~6.5 m. We therefore estimate a range of uncertainty on the scarp height at this location of 5.6 ± 1.5 m.

but not affected the uppermost units above that are dated to ~400 years B.P. by the preserved sedge bed. Wood and charcoal samples collected from two deformed sediment layers contained fern, gymnosperm, bark fragments, charcoal fragments, and horsetail (Equisetum). RC8 (gymnosperm) yielded an age of 5328–4931 calibrated radiocarbon years B.P. RC9 (horsetail) failed to yield a radiocarbon age. The soft-sediment deformation hence predates deposition of the uplifted sedge bed, and its formation is not related to the scarp-forming earthquake.

2.4.4. Southern Scarp Age

The southern scarp is preserved as an ~2 m step in Quaternary alluvium and can be traced westward for 3.6 km to 45°59′N/79°52′E where it ends (Figures 14 and 19). The scarp crossed the abandoned flood plain of the Lepsy River (Figures 14 and 19) but is not preserved in the bed of the most recent abandoned channel itself. Fault-parallel elevation profiles across this abandoned channel indicate that it is more deeply incised on the south side of the 2 m scarp than on the north side (Figure 19c) indicating that the river was able to continue flowing after this 2 m step-forming event and subsequently incised through the uplifted southern block. The 2 m high southern scarp, through which the river has been able to erode into and retain its course, hence formed in an earlier event (or events) than the main 5.6 ± 1.5 m high scarp, which postdated or was synchronous with deflection of the river, and abandonment of the channel.

Two luminescence samples, OSL7 and OSL8 (Table 1), were collected at depths of 0.30 m and 0.65 m respectively from a pit excavated into the abandoned channel on the downthrown north side of the southern scarp (Figure 19a). The stratigraphy revealed rounded, well-sorted, medium-grained quartz-rich river sands. OSL7 and OSL8 gave ages of 2245 ± 480 years and 1810 ± 400 years B.P., respectively. However, they are from the upper 1 m of fluvial sand and hence should be at a similar stratigraphic level to the sedge bed exposed at the quarry, within the same fluvial sequence, and which we dated using both radiocarbon and OSL to within the last ~400 years (RC5, RC7, and OSL6). We suggest that fluvial reworking of sediment from the incised upthrown side of the southern scarp has led to anomalously old ages for OSL7 and OSL8.

2.5. Possible Western Continuation of the Lepsy Fault

In addition to the 120 km of Holocene fault scarp, we suggest a possible geological continuation of the Lepsy fault for a further ~25 km west of the 5.6 ± 1.5 m scarp termination (shown as a purple line in Figure 2). However, we did not investigate this inferred continuation in the field, and we do not know if it shows evidence for Quaternary reactivation. The projected trace of the fault follows a linear color change in Quaternary sediment cover that may result from weathering of a subtle step in the landscape that is too small to resolve in 90 m resolution Shuttle Radar Topography Mission (SRTM) data (Figure 14b). In the far west at Kokterek town (~79°36′E, Figure 2), the westward flowing Lepsy River passes an apparent abandoned east flowing river channel preserved in the Goldybek Valley (Figure 2). At this abandoned confluence, outcrops of approximately E-W striking Paleozoic bedrock are observed, with apparent uplift to the north. This sense

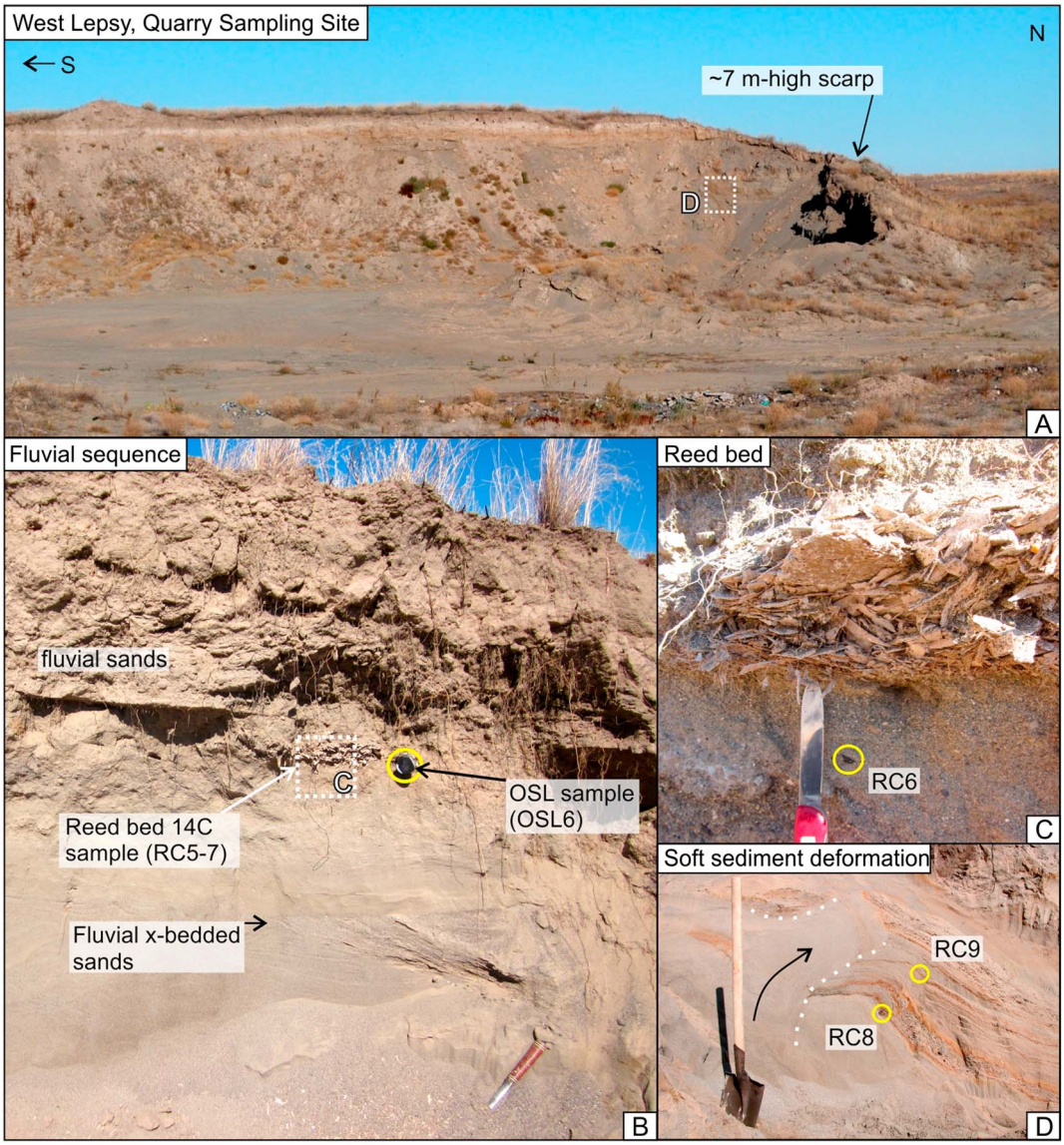

Figure 17. Quarry sampling site, west Lepsy. (a) View west of the quarry excavation, through the main scarp, which exposes a sequence of fluvial sands. The dashed white box shows the area of photo in Figure 17d. (b) Zoom of south facing exposure wall through the main scarp, showing cross-bedded fluvial sands, the location of the sedge bed preserved within the fluvial sequence (sample OSL7 and Table 1and samples RC5–RC7, Table 2). Dating materials from the sedge bed include Cyperaceae leaves (sedge plant family), with a mineral coating (likely to be related to the spring at this site along the fault, which has formed Ayak-Kol), wood, Pinus (conifer), and plant resin. (c) Close-up photo of the sedge bed, interpreted as a low-energy channel deposit. (d) Close-up photo of the sand boil soft-sediment deformation structure and location of radiocarbon samples RC8 (fern) and RC9 (gymnosperm charcoal) (Table 2). These radiocarbon samples include also unspecified bark fragments and equisetum (horsetail). The sand boil does not deform the overlying stratigraphy dated by samples RC5 and OSL6.

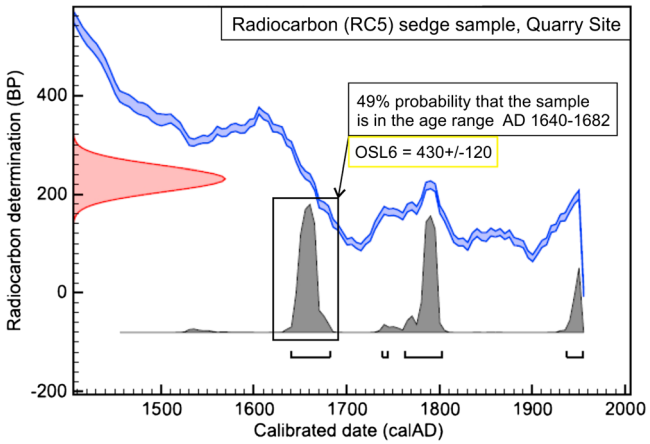

Figure 18. Radiocarbon sample RC5 (Cyperaceae leaves) from the sedge bed, west Lepsy quarry exposure. The left-hand axis shows radiocarbon concentration expressed in years "before present," and the bottom axis shows calendar years (derived from tree ring data). The pair of blue curves shows the radiocarbon measurements on the tree rings (plus and minus one standard deviation), and the red curve on the left indicates the radiocarbon concentration in the sample. The grey histogram shows possible ages for the sample (the higher the histogram, the more likely that age is). There is 95% confidence that the sample has an age range between AD 1640 and modern, with a 49% probability that its age is between A.D. 1640 and A.D. 1682. Sample OSL6, which was taken from fine quartz sands adjacent to the sedge bed, yielded an age of 430 ± 120. This independent age constraint provides confidence that the radiocarbon sample is in the older A.D. 1640 to A.D. 1682 age range (333–375 years B.P.).

of uplift is contrary to that mapped along the main Lepsy scarp but indicative of the predominant orientation of preexisting structure throughout this platform region.

3. Discussion

3.1. Kinematics

3.1.1. Fault Geometry and the Dominant Type of Faulting

Our observations and analysis of satellite imagery and fieldwork indicate that the overall sense of motion along the Lepsy fault is dip slip right lateral, with vertical motion as the dominant component in the east and with no direct constraint on horizontal motion in the west. In the Kazakh platform, the fault strikes WNW-ESE (~110–290°) and is hence likely to have a greater component of right-lateral strike slip than in its eastern section. This lateral motion is manifested in the left-stepping echelon pull-apart basins observed in the west (Figure 15). The Lepsy fault follows the dominant Palaeozoic structural trend, and it is likely that it represents a reactivated basement fault of the Kazakh platform [e.g., *Suvorov*, 1963, 1973; *Tapponnier and Molnar*, 1979; *Allen and Vincent*, 1997].

There is some ambiguity in trying to determine the fault dip direction, and hence the nature of fault motion, mainly because in the east the reactivated bedding dips very steeply, 80°N, and hence suggests a normal component. However, elsewhere several further observations, both at a regional scale and at a local scale, suggest that the fault is south dipping with a dominant reverse component. In particular, (1) earthquake mechanisms on E-W faults throughout the Tien Shan indicate dominantly reverse faulting consistent with N-S shortening (Figure 1); (2) these earthquake mechanisms are also consistent with a regional N-S shortening revealed by GPS measurements (Figure 1); (3) a fault dip of 50°S was observed close to the Tentek River site (Figure 10c); (4) the scarp is not likely to be a sackung [e.g., *Zischinsky et al.*, 1966; *Varnes et al.*, 1989; *Gutiérrez-Santolalla et al.*, 2005] as for most of its length it runs through the low-relief Kazakh platform (Figure 2); (5) reverse-faulted and folded Cenozoic red beds exposed at the Shingildy River immediately to the south of the scarp (Figure 13) suggest that the most recent period of activity in this region is compressional; and (6) in the east we infer that the fault has steepened at shallow depth to follow bedding, yielding an apparent north dip. Such depth-dependent variation in the type of fault is often observed in reverse-faulting earthquakes [e.g., *Yielding et al.*, 1981; *Liu-Zeng et al.*, 2010].

From the horizontal and vertical offset values (7 ± 2 m and 5–9 m, respectively) measured from our DEM at the Tentek River field site in Figures 10 and 11, the local fault strike of ~110° and using the ~50°S fault dip measured nearby (Figure 10c), we calculate a slip vector azimuth of 317° to 343°, which is similar to the azimuth of the GPS velocities relative to Eurasia that show NNW-SSE shortening at this latitude (~330°) (Figure 1). The overall fault motion is hence oblique reverse right lateral. From the measurements of fault dip, strike slip, and vertical slip we also calculate that 8.2–13.8 m of slip along the fault plane would be required to produce the observed vertical and lateral displacements across the scarp at the Tentek River site.

At its western end, the Lepsy scarp changes strike by 90° to trend N-S, and its height decays southward over a distance of ~22 km (Figures 2 and 14b). We interpret this terminal N-S fault to represent a tear, accommodating the uplift of the Lepsy fault hanging wall relative to the unfaulted plain to the west. Such orthogonal tear

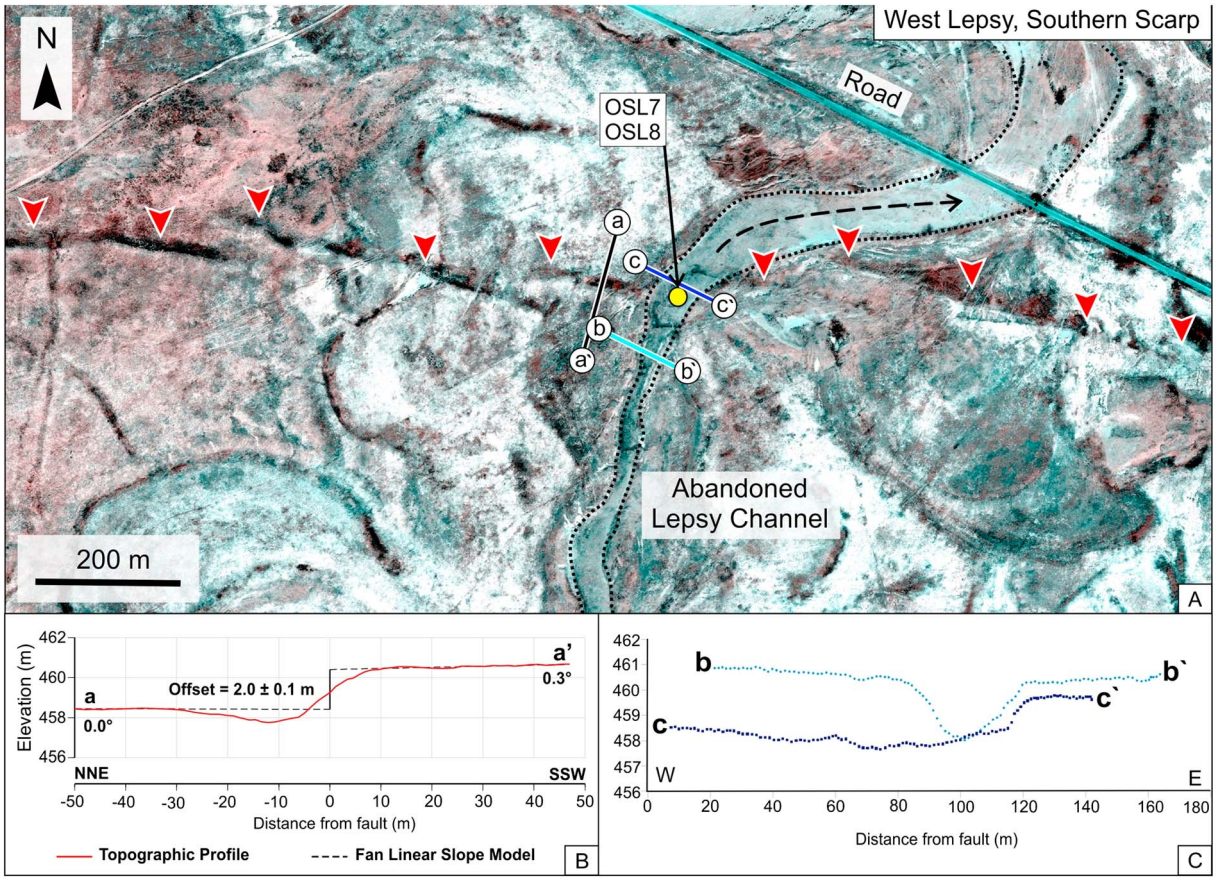

Figure 19. (a) Worldview satellite image of the subparallel southern fault scarp (see Figure 14 for image area location). Left-stepping segments of up to several hundred meters long are clear. The locations of samples OSL7 and OSL8 are shown (yellow circle). (b) DGPS scarp-perpendicular elevation profiles show 2 m of vertical offset (to which we add an uncertainty of ±1 m) preserved in late Quaternary fluvial deposits (profile line location shown in Figure 19a). (c) DGPS fault-parallel elevation profiles on either side of the fault show that the river continued flowing northward after this 2 m offset event. The hanging wall (south side) of the fault is more deeply incised (profile *b-b′*) than the north side (profile *c-c′*), which is consistent with uplift of the south side and continued northward river incision to reach an equilibrium base level.

fault terminations have been observed along other large intraplate reverse faults (e.g., the 1897 M_w 8.1 Assam earthquake, India [*Bilham and England*, 2001], the 1999 M_w 7.3 Chi Chi earthquake, Taiwan [*Lee and Shih*, 2011], and the 2008 M_w 7.9 Wenquan earthquake [*Xu et al.*, 2009]). The distance over which the vertical offset in the hanging wall of a fault decays is related to the depth extent of faulting [*Savage and Hastie*, 1966; *Wallace*, 1989; *Contreras et al.*, 2000]. In the case of the Lepsy fault, a depth extent of faulting of >20 km is consistent with well-constrained earthquake centroid depths, which indicate a seismogenic layer thickness of up to 40 km in the Kazakh platform (e.g., Figure 1). Alternatively, the geometry of the western Lepsy fault termination may be related to its strike-slip component. Similar fault terminations have been observed along other long intraplate faults with a strike-slip component elsewhere, for example, in Mongolia [*Bayasgalan et al.*, 1999] and Iran [*Berberian et al.*, 2000; *Walker et al.*, 2004; *Wesnousky*, 2005; *Hollingsworth et al.*, 2006]. The right-lateral component of motion and the fault configuration at the termination of the main Lepsy scarp are compatible with either interpretation.

Considering that the Lepsy fault seems to be a splay from the Dzhungarian fault, which extends into a low-relief part of the platform at its northern end, it is possible that the Lepsy fault has a similar role to that of the Dzhungarian fault. *Campbell et al.* [2013] determined a late Quaternary slip rate of 2.2 ± 0.8 mm/yr for the Dzhungarian fault and, using a simple kinematic model, determined that its slip rate is consistent with the accommodation of N-S shortening by counterclockwise rotation. The geometry of the Dzhungarian fault may, therefore, indicate that both right-lateral strike-slip and counterclockwise rotations about a vertical axis play a role in accommodating N-S shortening in the northern Tien Shan. Vertical axis block rotations have been documented in many places around the world and have been shown to be an efficient mechanism to

Journal of Geophysical Research: Solid Earth

10.1002/2015JB011925

Table 1. Luminescence Ages for the Lepsy Fault

						Radioisotopes[b]						
Labcode	Site	Latitude	Longitude	Depth (m)	Water[a] (%)	K (%)	Th (ppm)	U (ppm)	Cosmic (Gy/ka)	Total Dose Rate (Gy/ka)	D_e[c] (Gy)	OSL Age[d] (ka)
X6030[e]	(OSL1) Jaxa-Kol	45°55′07.80	81°25′51.56	0.85	7.6	2.88	9.0	3.1	0.24 ± 0.03	3.98 ± 0.24	7.04 ± 2.00	1.77 ± 0.51
X6031[e]	(OSL2) Jaxa-Kol	45°55′18.96	80°34′20.76	0.65	10.6	2.84	10.1	3.0	0.25 ± 0.04	3.86 ± 0.23	3.50 ± 2.01	0.91 ± 0.52
X6019	(OSL3) Shingildy	45°55′18.96	80°34′20.76	1.05	1.8	2.56	6.0	1.4	0.20 ± 0.02	3.30 ± 0.21	7.23 ± 1.48	2.19 ± 0.47
X6018	(OSL4) Shingildy	45°55′18.96	80°34′20.76	1.55	0.9	2.17	5.8	1.6	0.20 ± 0.02	2.97 ± 0.18	14.88 ± 1.84	5.01 ± 0.70
X6020	(OSL5) Pull-apart basin	45°59′08.63	79°58′00.17	0.60	5.7	2.24	7.1	1.5	0.21 ± 0.04	2.93 ± 0.18	0.87 ± 0.43	0.30 ± 0.15
X6023	(OSL6) Quarry, sedge bed	45°59′08.63	79°58′00.17	0.80	7.2	2.40	6.4	1.6	0.20 ± 0.03	2.97 ± 0.19	1.27 ± 0.36	0.43 ± 0.12
X6021	(OSL7) Channel	45°59′08.63	79°58′00.17	0.30	0.3	2.12	6.8	1.8	0.22 ± 0.05	3.05 ± 0.20	6.85 ± 1.38	2.24 ± 0.48
X6022	(OSL8) Channel	45°59′08.63	79°58′00.17	0.65	8.9	2.65	5.3	1.2	0.21 ± 0.03	3.03 ± 0.20	5.49 ± 1.15	1.81 ± 0.40

[a] Measured water contents are expressed as a percentage of the dry mass of the sample. A long-term mean water content of 3.0 ± 3.0% was assumed for the dose rate determinations of samples X6018, X6019, and X6021.

[b] Measurements were made on dried, homogenized, and powdered material by ICP-MS/AES with an assigned systematic uncertainty of ±5%. Dry beta dose rates calculated from these activities were adjusted for the field water content.

[c] OSL measurements were made with an automated TL/DA-15 Risø luminescence reader [*Bøtter-Jensen*, 1997; *Bøtter-Jensen et al.*, 2000] and conducted on 180–250 μm diameter quartz grains mounted as multigrain aliquots. The equivalent dose (D_e) was obtained using a single-aliquot regeneration measurement protocol [*Murray and Wintle*, 2000; *Wintle and Murray*, 2006].

[d] The age datum refers to A.D. 2013 when the samples were measured and the luminescence dates are based on central age model estimates of the weighted mean D_e values. The total uncertainty (1σ), calculated as the quadratic sum of the random and systematic errors, includes all measurement uncertainties as well as a relative error of 2% to account for possible bias in the calibration of the laboratory beta source.

[e] OSL samples X6030 and X6031 had low quartz sensitivity. The dose rates of these samples rely on a small number of measurements, hence the relatively larger error estimates for these samples.

Table 2. Radiocarbon Material, Ages, and Calibration for Samples Collected Along the Lepsy Fault[a]

Lab Code[a]	Site	Latitude	Longitude	Material	^{14}C Age (B.P.)[b,c]	Calibrated Range (95%)[d]	Age (Cal Years B.P.)
OxA-27911	(RC1) Jaxa-Kol	45°55′07.80	81°02′51.56	Organic-rich soil	1, 904 ± 26	A.D. 75 to A.D. 209	1,988–1,806
OxA-27910	(RC2) Shingildy	45°55′18.96	80°34′20.76	Charred gravel	–	–	–
OxA-27700	(RC3) Pull-apart basin	45°59′08.63	79°58′00.17	Charcoal (gymnosperm, small branch)	351 ± 24	A.D. 1482 to A.D. 1626	558–380
OxA-27909	(RC4) Pull-apart basin	45°59′08.63	79°58′00.17	Grass stems and leaves	–	–	–
OxA-27701	(RC5) Quarry A	45°59′57.60	79°54′25.16	Cyperaceae leaves (sedges), with mineral coating	231 ± 26	A.D. 1640 to modern	375 to modern
OxA-29866	(RC6) Quarry B	45°59′57.60	79°54′25.16	Plant resin	>57,800		
OxA-29383	(RC7) Quarry Aa	45°59′57.60	79°54′25.16	Wood: Pinus (conifer)	149 ± 24	A.D. 1667 to A.D. 1949	348–66
OxA-27702	(RC8) Quarry C	45°59′57.60	79°54′25.16	Plant remains (fern)	4, 409 ± 33	B.C. 3,313 to B.C. 2,916	5,328–4,931
P-33197	(RC9) Quarry D	45°59′57.60	79°54′25.16	Gymnosperm charcoal, Equisetum (horsetail)	–	–	–

[a]Samples prepared and run at the accelerator mass spectroscopy, Research Laboratory for Archaeology and the History of Art, University of Oxford. For details of the chemical pretreatment, target preparation and AMS measurement, see *Radiocarbon* 46 , 17–24 and 155–63, and *Archaeometry44* (3 Supplement 1) and 1–149.
[b]Delta ^{13}C values are measured independently on a stable isotope mass spectrometer (to ± 0.3‰ relative to VPDB).
[c]The quoted ages are in radiocarbon years using the Libby half-life of 5568 years.
[d]Calibration with IntCal13: Northern Hemisphere [after *Reimer et al.*, 2013].

accommodate and transfer strain on the continents [e.g., *Freund*, 1970; *Ron et al.*, 1984; *McKenzie and Jackson*, 1986; *Nur et al.*, 1986; *Jackson and Molnar*, 1990; *Goldsworthy et al.*, 2002; *Walker and Jackson*, 2004]. In the northern Tien Shan, without better GPS coverage and paleomagnetic data, it is difficult to further quantify the role of the Lepsy fault in accommodating N-S shortening by vertical axis rotation.

3.2. Earthquake Chronology, Scaling, and Magnitudes

In this section we use our observations of the geomorphology in combination with OSL and radiocarbon ages to discuss the possible seismic history of the Lepsy fault. We then use the mapped sense of offset, the lateral extent of surface faulting, and the measurements of slip to speculate on potential earthquake magnitudes.

3.2.1. Seismic History

Our dating indicates evidence for at least two substantial earthquakes along the Lepsy fault during the Holocene. In the west, a 5.6 ± 1.5 m vertical scarp at the quarry site (Figures 14 and 16) appears to have formed since ~400 years B.P. We suggest that this 4–7 m scarp was generated by a single large earthquake in the early part of this age range, rather than by multiple earthquakes within the last 400 years, as it is more consistent with the lack of documented historical earthquakes in this region [*Mushketov*, 1785]. If the 5.6 ± 1.5 m scarp at Ayak-Kol formed in a single earthquake, then the Lepsy River may well have been diverted from its course by this event. The hanging wall is on the southern, upstream, side of the fault, and considering that hanging wall uplift is typically 10 times footwall subsidence in large reverse-faulting earthquakes [*Oglesby et al.*, 1998], the river would have experienced a significant decrease in the gradient of the river. Given that it is sited in the low-relief Kazakh platform, if any slip failed to reach the surface, additional folding and warping of the hanging wall (e.g., as observed in the Coalinga, Northridge, and Tabas earthquakes) [*Berberian*, 1979; *Stein and King*, 1984; *Hauksson et al.*, 1995] could also cause the same significant decrease in the gradient of the river. In the very low relief of the Kazakh platform this decrease in gradient would have affected the flow of the river and may have prompted the river to change its course.

South of the quarry site, a second parallel scarp ~2 m high must date from an earlier event, as the Lepsy River eroded through this offset and was not diverted from its N-S course until later, but prior to the last earthquake. Therefore, where the northern (5.6 ± 1.5 m high) and southern (2 ± 1 m high) fault scarps merge to form a single 9–10 m high scarp, we know that this maximum offset did not occur in a single earthquake, at least in the west, despite forming a single steep and continuous scarp. Following this reasoning, it is not clear whether the scarps we observed farther east were generated by a single event or whether they are composite scarps formed in multiple events. The older 2 m step-forming event, or other events, may contribute to the observed scarp heights in these more easterly sections. The Tentek River site (section 2.3.3) is the only location other than Ayak-Kol where we are confident from our interpretation of the geomorphology that the scarp was

formed in a single event. We note that there are two parallel scarps visible in the geomorphology adjacent to the western bank of the Tentek River (Figure 10), and we speculate that these two scarps represent ruptures from two separate earthquakes.

We have no direct constraint on the age of the ~2 m high scarp at Ayak-Kol, other than it is older than 400 years (section 2.4), though it may be related to soft-sediment deformation we found in fluvial sediments exposed in the Ayak-Kol quarry, and dated to less than ~5000 years. It is unclear whether the penultimate event at the western quarry site ruptured most of the length of the Lepsy fault or whether the fault ruptured in a number of smaller events along its length. In the easternmost section of the fault, near Jaxa-Kol, an earthquake must have occurred before ~2000 years B.P. in order for sediments to be ponded at the scarp (section 2.2). Also, at the Shingildy River initial uplift of the lowest observed terrace occurred between $\sim 5 \pm 0.7$ and 2.2 ± 0.5 ka. Scarp formation along these eastern and central fault sections may be related to the same older event scarp observed in the west or may relate to other older events.

3.2.2. Fault Scaling and Potential Earthquake Magnitudes

Our observations of the geomorphology and age control indicate that the Lepsy fault has generated at least two large earthquakes in the Holocene. The fault scarp appears very fresh along its entire length, from which we infer that it has been reactivated along its entire length in the recent past, but for most of its length the scarp is likely to represent cumulative displacement in at least two earthquakes. However, we have identified two sites where the geomorphology suggests displacement arising solely from a single earthquake. The first of these sites is at the Tentek River, where we were able to estimate 8.2–13.8 m of slip with an azimuth of 317–343°. The second location is at Ayak-Kol, near the western end of the fault, where we interpret a 5.6 ± 1.5 m vertical scarp to have formed in a single earthquake within the last ~400 years. We have no direct measurement of fault dip in this western area, and so to estimate the slip along the fault plane at Ayak-Kol, we assume that it is unchanged from the 50°S measured in the Tentek River gorge in the east. Taking that fault dip, the slip vector azimuth of 317–343°, and the local fault trend of 110° at Ayak-Kol, we estimate between 2.6 m and 11.6 m of right-lateral strike slip at Ayak-Kol and a total slip along the fault plane of 6 m to 14.7 m. We suspect that the fault dip is not particularly gentle due to the large component of strike slip. If the local dip is steeper, the total slip will be smaller.

If our interpretations are correct, the ~120 km length of the Lepsy fault ruptured in the last 400 years in a single event with slip of 8.2–13.8 m. Given the 120 km length, our estimates yield a slip to length ratio of $\sim 10^{-4}$, which is larger than the majority of global earthquakes [*Wells and Coppersmith*, 1994], but examples with similar ratios are known. Most recently, the M_w 7.6 2001 Bhuj earthquake in India involved slip of ~10 m on a rupture with a length of only 20–30 km by 20 km [*Schmidt and Bürgmann*, 2006; *Copley et al.*, 2011]. The 1897 M_w 8.1 Assam earthquake, India, is also thought to have involved slip of 11–25 m of slip on a fault 110 km in length [*Bilham and England*, 2001]. Well-constrained prehistoric examples also exist, for example, the ~4 ka Egiin Davaa paleo-earthquake rupture in Mongolia, which involved almost uniform slip of ~8 m along an 80 km length [*Walker et al.*, 2015]. These examples are all from intraplate regions, where the seismogenic thickness may be larger than typical, and the large slip at Lepsy may be related to the structural immaturity of the fault, which appears to be a major factor in controlling the magnitude of slip in an earthquake, with "immature" faults tending to fail in shorter though more energetic ruptures [*Manighetti et al.*, 2007].

To estimate the magnitude of this event, we use the empirical relationships of *Wells and Coppersmith* [1994]. We have only two estimates of the slip in the most recent earthquake and so perform a range of calculations making either the assumption that the slip of ~8–14 m at the Tentek River site represents the maximum surface slip or considering that the scarp height is similar at sites in both the east and west, and to acknowledge that not all slip may have reached the surface, we also calculate the magnitude using 8–14 m as an average slip. Applying the scaling relationship between M_w (moment magnitude) and fault displacement yields an M_w of 7.5–7.7 using the mean coefficients for strike-slip faulting. Treating the 8–14 m as a maximum slip yields a magnitude of 7.8–8.1. Applying the scaling relationship between M_w (moment magnitude) and rupture length (120 km) yields an M_w of 7.5 using the mean coefficients for strike-slip faulting. We also calculate seismic moment (M_o) using the relationship $M_o = \mu A \bar{u}$ [*Scholz*, 1982], assuming a value of 3×10^{10} Nm^{-2} for the shear modulus (μ), slip ($\bar{u}$) of either 8 or 14 as above, and a rupture area (A) computed from a scarp length of 120 km, a fault dip of 50°, and a range of seismogenic depths. With a mean slip of 8 m, we estimate seismic moment between 7.5×10^{20} Nm and 1.3×10^{21}, depending on whether the seismogenic depth is taken to be 20 km or 35 km, which in turn yield moment magnitudes of M_w 7.8–8.0. Using slip of 14 m, the

same calculations yield seismic moments between 1.31×10^{21} Nm and 2.27×10^{21} and moment magnitudes of M_w 8.1–8.2.

The oldest event described in the documented historical record for the region [*Mushketov and Orlov*, 1893] indicates that a large earthquake, located in the Dzhungaria region of SE Kazakhstan, in the vicinity of Lake Balkhash, occurred in 1715. Assuming that our magnitude estimate for the most recent earthquake on the Lepsy fault is correct (M_w 7.5–8.2) and that it occurred sometime in the last 400 years, this documented historical earthquake of 1715 may be a candidate for the last earthquake on the Lepsy fault.

3.3. Implications for Faulting in Intraplate Regions

The Tien Shan is one of the most seismically active intracontinental mountain belts in the world, with many earthquakes occurring on reactivated faults within the high mountains, where rates of shortening are fastest (e.g., ~15–20 mm/yr; Figure 1). Less well known are the rare earthquakes that occur in the Tien Shan foreland, where rates of shortening are much less (≤2 mm/yr). The Lepsy fault provides a clear example, through its ~10 m high Holocene escarpment, of a fault that extends from the more rapidly deforming mountainous region to the slowly deforming foreland. The fault appears to follow a Palaeozoic structure, and given that along the western half of the scarp there is relatively little evidence for Cenozoic reactivation other than the ~10 m scarp, we suggest that it has been reactivated relatively recently. There is evidence that the geological Lepsy fault continues even farther west into the low strain rate platform, though we do not know whether these sections have been active in the Quaternary. It is possible that other structures within the mountain ranges of central Asia may actually extend into regions that are thought of as "stable" and that these structures may also remain active in the Quaternary, but we are unable to observe them because the long recurrence times allow processes of erosion and/or deposition that remove or bury the expression of surface faulting in the landscape [e.g., *Walker et al.*, 2008, 2013].

In summary, there are two key issues. First is whether low strain rate continent interiors should always be thought of as stable, considering their potential for large unexpected earthquakes, as evidenced by this study and a growing number of studies from other apparently aseismic continent interiors worldwide [e.g., *Crone and Luza*, 1990; *Walker et al.*, 2008; *Clark et al.*, 2012, 2013; *Copley et al.*, 2014]. Second is whether our framework for viewing such earthquakes is one of isolated seismogenic faults within absolutely stable and undeforming continental interiors or whether these faults are on a network of interconnected faults, perhaps linked to a distant, more rapidly deforming region, but whose connectivity is obscured by erosional and depositional processes operating rapidly compared to the long earthquake recurrence times.

4. Conclusions

Our observations and analysis of satellite imagery and fieldwork indicate that the Lepsy fault is a reverse right-lateral fault that extends approximately E-W for ~120 km from the mountains of the Dzhungarian Ala-tau, in the northern Tien Shan, into the low-lying Kazakh platform. Dating of the most recent surface faulting events on the Lepsy fault suggests that two large earthquakes have occurred: the first, since at least 5000 years B.P. in the west, and the second, after ~400 years B.P., in an event which likely ruptured the entire ~120 km fault length. Earthquake scaling relationships suggest that the last event would have generated a maximum magnitude M_w 7.5–8.2 earthquake. Although the documented historical earthquake record for this region is relatively short (several hundred years), this last earthquake may correspond to a large destructive earthquake that occurred in 1715 in the region of Lake Balkhash, Dzhungaria.

The Holocene activity on the Lepsy fault illustrates two important points: (1) the fact that large-magnitude earthquakes can and do occur in regions that have been free of large earthquakes in the instrumental period, such as the Kazakh platform, and provide a reminder that seismic behavior should be assessed over much longer periods of time when considering long-term deformation and associated seismic hazard, and (2) the example of the Lepsy fault reveals that structures in regions that are considered stable may be connected directly with distant, more rapidly deforming regions and may follow networks of interconnected faults inherited from earlier tectonic periods.

Appendix A: Estimation of Vertical and Lateral Displacements

The measurements of vertical and horizontal displacements across the Lepsy scarps are important both for estimating the direction of slip and also for estimating the amount of slip required to produce the

observed scarp. The uncertainty in displacement can be estimated by taking multiple topographic profiles at many sites. However, the field surveys that we present in this paper form a reconnaissance that was performed in a relatively short time and with restricted access along much of the fault length. Here we briefly describe the approaches we took in measuring the vertical and strike-slip components of slip at those sites where we were able to doso.

Vertical fault offsets at each DGPS-surveyed site (with the exception of Figure 5, which was interpolated from the gridded DEM) were calculated from a linear inversion of the profile points sited at a distance from the degraded scarp [e.g., *Walker et al.*, 2015]. Typically, only points measured beyond 15–30 m on either side of the fault scarp were used in the offset/slope calculations, with the choice of offset distance chosen on a case-by-case basis. For instance, in Figure 19, a wide shallow depression is present at the base of the scarp, and survey points within this depression were not used in the calculation. On longer profiles, heights beyond where the fan slope flattens downslope or steepens upslope are discounted. A value of vertical displacement is then calculated at the midpoint of the scarp, where the scarp gradient is greatest. The error on the vertical displacement is estimated from the fit of the modeled upper and lower surfaces and includes a weighting of the GPS points assuming a constant error of 6 cm for each. (The reported error in the heights of the individual points on the DGPS profiles is variable but typically within ~5–6 cm.) The errors reported from this approach, though relatively small, do not account for uncertainties arising from changes in gradient between the upper and lower surfaces nor do they account for variability in scarp height along strike. In the text we hence apply a uniform uncertainty of ± ~1 m to all measurements of vertical displacement, as this range encompasses the range of heights. Exceptions are the scarps shown in Figures 5, 10, and 15, where variability between displacement measurements on duplicate closely spaced profiles exceeds 2 m and may reflect a real variation of vertical displacement along strike. In these cases we assign an uncertainty that is sufficient to cover the range of heights measured from each set of closely spaced profiles.

Lateral offsets were estimated at the few sites where we were able to observe well-defined ridge crests or fluvial risers that are orthogonal to the fault trace. It is necessary to only attempt lateral reconstructions where the offset landform is orthogonal to the fault scarp, as the large shortening component would introduce apparent lateral displacements of any nonorthogonal feature. To estimate lateral displacement, we first gridded individual DGPS survey points to produce digital elevation models (with a pixel spacing of ~50 cm). Topographic profiles parallel to the fault, and on either side of it, were then extracted from the DEM. A piercing point for the channel thalweg or ridge crest was determined on either side of the fault by projecting the channel slopes to a crossover point. Lateral offsets were then estimated visually by realigning the piercing points. For each measurement of lateral displacement we show the original topographic profiles, the profiles with lateral displacement restored, and also a panel with the vertical displacement removed to provide a visual measure of the degree of fit. For each measurement of lateral displacement we state a conservative uncertainty of ±2 m, as outside this range there is a visible degradation in the restoration.

Appendix B: Quaternary Dating Methods

In total, 17 samples were dated. Nine of these samples were collected for radiocarbon dating, which provides an age on organic material incorporated within the sediment layers. Eight samples were collected for optically stimulated luminescence (OSL), which determines the time at which quartz-bearing sediment was last exposed to sunlight. Where possible, both radiocarbon and OSL samples were collected at the same site for age comparison, and we found good agreement in the three sites where we used both dating methods. OSL and radiocarbon ages and sample details are reported in Tables 1 and 2, respectively. Detailed descriptions of the dating sites, the sample context, and sample materials are provided on a site-by-site basis.

B1. Radiocarbon

All radiocarbon samples were collected either from newly dug excavations or from refreshed cuttings. Samples were extracted from the sediment and collected either in glass vials or in metal foil, which were then placed in sealed plastic sample bags. Prior to analysis, all plant material was identified, any root material or other contaminants removed, and if possible the most rapid growing species selected from each site to reduce the potential for inheritance (S. Harris, Oxford University, personal communication, 2013). Radiocarbon dating was performed at the University of Oxford, following the standard procedures for chemical pretreatment, target preparation, and AMS measurement given in *Radiocarbon46* (1), 17–24 and 155–63, and *Archaeometry44* (3 Supplement 1), 1–149. Isotopic fractionation has been corrected for using the measured δ13C values measured on the accelerator mass spectrometer. The quoted δ13C values are measured

independently on a stable isotope mass spectrometer (to ±0.3‰ relative to Vienna Peedee belemnite (VPDB)). Uncalibrated ages are given in radiocarbon years B.P. (B.P. to A.D. 1950) using the half-life of 5568 years. Calibrations were performed using Oxcal (v4.2) of *Bronk* [1994], using the "INTCAL13" data set [*Reimer et al.*, 2013].

B2. OSL

The OSL samples were collected in steel tubes, hammered into the sediment, and sealed at the ends with layers of metal foil and opaque tape. The samples were opened and prepared under low-intensity light-emitting diode lighting (emitting at ~588 nm). Sediment in the outer thirds of each tube was removed and used for dose rate measurements. The inner third of the sediment was prepared for dating. The OSL sample preparation and analysis procedures are as reported in *Campbell et al.* [2013]. The dating was performed at the University of Oxford and was based on quartz grains extracted from the sediment samples. Laboratory procedures were designed to yield clean, sand-sized (180–250 μm) grains of quartz for optical dating according to standard preparation methods, including wet sieving, HCl acid digestion, heavy liquid flotation using sodium polytungstate, and etching in concentrated hydrofluoric acid (40%) to dissolve potassium feldspar minerals and to clean and remove the outer alpha-dosed layer of quartz grains. The latter residual grains were resieved to the original grain size range and mounted as multigrain monolayers of approximately 4 mm diameter onto aluminium disks using a silicone oil adhesive. To determine the equivalent dose (D_e), a single-aliquot regeneration measurement protocol was used [*Murray and Wintle*, 2000; *Wintle and Murray*, 2006] and OSL measurements were conducted using an automated TL/DA-15 Risøluminescence reader [*Bøtter-Jensen*, 1997; *Bøtter-Jensen et al.*, 2000]. Optical stimulation for single aliquots was provided by clusters of blue light-emitting diodes (42 Nichia 470 nm) providing a sample stimulation power of >80 m W cm^2.

The natural and regenerative doses were preheated at 26°C for 10 s, and the fixed test doses (which are used to correct for any sensitivity changes) were preheated at a reduced temperature of 240°C for 10 s, before optical stimulation. The absence of infrared-sensitive minerals (e.g., feldspars) was checked and confirmed using an infrared bleach (50 s) provided by clusters of 870 nm IR light-emitting diodes providing >135 m W/cm^2 a solid-state laser diode (83,010 nm; 1 W cm^2) at 50°C for 100 s before blue light stimulation [*Banerjee et al.*, 2001]. The ultraviolet OSL emission at 370 nm was detected using an Electron Tubes Ltd. 9235QB15 photomultiplier tube fitted with a blue-green sensitive bialkali photocathode and 7.5 mm of Hoya U-340 glass filter. Laboratory doses used for constructing dose response curves were given using a calibrated ^{90}Sr/^{90}Y beta source housed within the reader. At least 12 disks were prepared from each sample, except for samples OSL1 and OSL2, as marked in Table 1. Following measurement of the natural signal, a dose response curve was constructed from six to eight dose points including a zero dose point and a replicate measurement of the lowest regenerative dose.

The environmental gamma and beta components of the dose rate result from the radioactive decay series of ^{238}U, ^{232}Th, and ^{40}K within the sediment. The concentrations of these parent isotopes were obtained by inductively coupled plasma mass spectroscopy (ICP-MS/AES) using a lithium metaborate/tetraborate fusion. These concentrations were converted to dose rates according to attenuation factors proposed by *Adamiec and Aitken* [1998], using corrections for grain size [*Mejdahl*, 1979] and water content [*Zimmerman*, 1971]. The cosmic ray dose was calculated according to standard data reported by *Prescott and Hutton* [1994], taking into account the height and density of the overburden, as well as the geomagnetic latitude and elevation of the site. Quartz yields and sensitivities were low for two samples (OSL1 and OSL2), which would decrease confidence in the ages obtained for these two, but radiocarbon samples taken from the same sample pit give concordant ages.

Acknowledgments

We thank NERC for a small grant (NE/G010978/1) awarded to R.T.W. and the Royal Society International Travel Grant, Mike Coward Fund of the Geological Society of London, Percy Sladen Fund of the Linnean Society, the Gilchrist Educational Trust, and the Earth and Space Foundation for their support in funding the field component of this project. G.E.C.'s doctoral studentship is funded by the National Environmental Research Council (NERC). R.T.W. is supported by a University Research Fellowship awarded by the Royal Society. We also thank the National Centre for Earth Observation (NCEO), the Centre for the Observation and Modelling of Earthquakes, Volcanoes and Tectonics (COMET+), and the NERC-ESRC funded project, Earthquakes without Frontiers (EwF), all of which have contributed to the funding of this project. DigitalGlobe high-resolution satellite imagery was obtained from Google Earth (www.earth.google.co.uk/). Shuttle Radar Topography Mission (SRTM) was obtained from CGIAR-CSI. We thank Barry Parsons, Oxford University, for providing Worldview satellite imagery, through COMET+. Great thanks to Ivan, Atyr, and Ainagul for their support in the field and helping with the logistics of the fieldwork and to Natalya Mikhailova at the Kazakhstan National Data Centre (KNDC). This work benefited from discussions with Magali Rizza, Jeff Ritz, and Tom Rockwell. We also thank T. Higham and R. Staff at the Research Laboratory for Archaeology and the History of Art, Oxford, for their help with radiocarbon sample preparation and analysis and S. Harris at the Department of Plant Sciences, University of Oxford, for his expertise in identifying our organic sample material. We thank Olaf Zielke, an anonymous reviewer, and the Associate Editor for their detailed comments that have led to a much improved paper.

References

Abdrakhmatov, K., et al. (1996), Relatively recent construction of the Tien Shan inferred from GPS measurements of present-day crustal deformation rates, *Nature*, *384*, 450–453.

Abdrakhmatov, K., K. D. Djanuzakov, and D. Delvaux (2002), Active tectonics and seismic hazard of the Issyk-Kul basin in the Kyrgyz Tian-Shan, in *Lake Issyk-Kul: Its Natural Environment*, vol. 13, edited by J. Klerkx and B. Imanackunov, pp. 147–160, NATO Science Series IV, Earth and Environmental Sciences, Kluwer Acad., Dordrecht, Netherlands.

Abdrakhmatov, K. Y., R. J. Weldon, S. C. Thompson, D. W. Burbank, C. Rubin, M. M. Miller, and P. Molnar (2001), Onset, style and current rate of shortening in the central Tien Shan, Kyrgyz Republic, *Geol. Geofiz.*, *42*, 1585–1609.

Adamiec, G., and M. Aitken (1998), Dose-rate conversion factors: New data, *Ancient Therm. Lum.*, *16*(2), 37–50.

Allen, M. B., and S. J. Vincent (1997), Fault reactivation in the Junggar region, northwest China: The role of basement structures during Mesozoic-Cenozoic compression, *J. Geol. Soc. London*, *154*(1), 151–155.

Arrowsmith, J. R., C. J. Crosby, A. M. Korjenkov, E. Mamyrov, and I. E. Povolotskaya (2004), Surface rupture along the Chon Aksu and Aksu (eastern) segments of the 1911 Kebin (Chon-Kemin) earthquake, Tien Shan, Kyrgyzstan, *Eos Trans. AGU*, *85*(47). Fall Meet. Suppl., Abstract T14C-02.

Avouac, J. P., P. Tapponnier, M. Bai, H. You, and G. Wang (1993), Active thrusting and folding along the northern Tien Shan and late Cenozoic rotation of the Tarim relative to Dzungaria and Kazakhstan, *J. Geophys. Res.*, *98*(B4), 6755–6804.

Banerjee, D., A. S. Murray, L. Bøtter-Jensen, and A. Lang (2001), Equivalent dose estimation using a single aliquot of polymineral fine grains, *Radiat. Meas.*, *33*(1), 73–94.

Bayasgalan, A., J. Jackson, J. F. Ritz, and S. Carretier (1999), Field examples of strike-slip fault terminations in Mongolia and their tectonic significance, *Tectonics*, *18*(3), 394–411.

Berberian, M. (1979), Earthquake faulting and bedding thrust associated with the Tabas-e-Golshan (Iran) earthquake of September 16, 1978, *Bull. Seismol. Soc. Am.*, *69*(6), 1861–1887.

Berberian, M., J. A. Jackson, M. Qorashi, M. Talebian, M. Khatib, and K. Priestley (2000), The 1994 Sefidabeh earthquakes in eastern Iran: Blind thrusting and bedding-plane slip on a growing anticline, and active tectonics of the Sistan suture zone, *Geophys. J. Int.*, *142*(2), 283–299.

Bilham, R., and P. England (2001), Plateau pop-up during the 1897 Assam earthquake, *Nature*, *410*, 806–809.

Bogdanovich, K. I., I. M. Kark, B. Y. Korol'kov, and D. I. Mushketov (1914), *Earthquake in Northern District of Tien Shan, 22 December 1911 (4 January 1911), in Russian*, Commission of the Geology Committee, St. Petersburg.

Bøtter-Jensen, L. (1997), Luminescence techniques: Instrumentation and methods, *Radiat. Meas.*, *27*(5–6), 749–768.

Bøtter-Jensen, L., E. Bulur, G. A. T. Duller, and A. S. Murray (2000), Advances in luminescence instrument systems, *Radiat. Meas.*, *32*(5), 523–528.

Bronk, R. C. (1994), Analysis of chronological information and radiocarbon calibration: The program OxCal, *Archaeological Comput. Newslett.*, *41*, 11–16.

Burbank, D. W., J. K. McLean, M. Bullen, K. Y. Abdrakhmatov, and M. M. Miller (1999), Partitioning of intermontane basins by thrust-related folding, Tien Shan, Kyrgyzstan, *Basin Res.*, *11*(1), 75–92.

Burtman, V. S., S. F. Skobelev, and P. Molnar (1996), Late Cenozoic slip on the Talas-Ferghana fault, the Tien Shan, central Asia, *Geol. Soc. Am. Bull.*, *108*(8), 1004–1021.

Campbell, G. E., R. T. Walker, K. Abdrakhmatov, J. L. Schwenninger, J. Jackson, J. R. Elliott, and A. Copley (2013), The Dzhungarian fault: Late Quaternary tectonics and slip rate of a major right-lateral strike-slip fault in the northern Tien Shan region, *J. Geophys. Res. Solid Earth*, *118*, 1–18, doi:10.1002/jgrb.50367.

Chediya, O. K. (1986), *Morphostructure and Neo-Tectonics Structure of the Tien Shan*, Academia Nauk Kyrgyzs CCP Frunze, Frunze.

Chen, W.-P., and P. Molnar (1977), Seismic moments of major earthquakes and the average rate of slip in central Asia, *J. Geophys. Res.*, *82*(20), 2945–2969.

Clark, D., A. McPherson, and R. Van Dissen (2012), Long-term behaviour of Australian stable continental region (SCR) faults, *Tectonophysics*, *566*, 1–30.

Clark, D., A. McPherson, T. Allen, and M. De Kool (2013), Coseismic surface deformation caused by the 23 March 2012 Mw 5.4 Ernabella (Pukatja) Earthquake, Central Australia: Implications for fault scaling relations in cratonic settings, *Bull. Seismol. Soc. Am.*, *104*(1), 24–39.

Contreras, J., M. H. Anders, and C. H. Scholz (2000), Growth of a normal fault system: Observations from the Lake Malawi basin of the east African rift, *J. Struct. Geol.*, *22*(2), 159–168.

Copley, A., J. P. Avouac, J. Hollingsworth, and S. Leprince (2011), The 2001 Mw 7.6 Bhuj earthquake, low fault friction, and the crustal support of plate driving forces in India, *J. Geophys. Res.*, *116*, B08405, doi:10.1029/2010JB008137.

Copley, A., J. Hollingsworth, and E. Bergman (2012), Constraints on fault and lithosphere rheology from the coseismic slip and postseismic afterslip of the 2006 M_w 7. 0 Mozambique earthquake, *J. Geophys. Res.*, *117*, B03404, doi:10.1029/2011JB008580.

Copley, A., S. Mitra, R. A. Sloan, S. Gaonkar, and K. Reynolds (2014), Active faulting in apparently stable peninsular India: Rift inversion and a Holocene-age great earthquake on the Tapti Fault, *J. Geophys. Res. Solid Earth*, *119*, 6650–6666, doi:10.1002/2014JB011294.

Crone, A. J., and K. V. Luza (1990), Style and timing of Holocene surface faulting on the Meers fault, southwestern Oklahoma, *Geol. Soc. Am. Bull.*, *102*(1), 1–17.

Cunningham, D., L. A. Owen, L. W. Snee, and L. Jiliang (2003), Structural framework of a major intracontinental orogenic termination zone: The easternmost Tien Shan, China, *J. Geol. Soc. London*, *160*(4), 575–590.

Delvaux, D., K. E. Abdrakhmatov, I. N. Lemzin, and A. L. Strom (2001), Landslide and surface breaks of the 1911 M 8.2 Kemin earthquake, *Landslides*, *42*(10), 1583–1592.

Engdahl, E. R., R. van der Hilst, and B. Raymond (1998), Global teleseismic earthquake relocation with improved travel times and procedures for depth determination, *Bull. Seismol. Soc. Am.*, *88*(3), 722–743.

Everingham, I. B., and P. J. Gregson (1969), Thrust fault scarp in the Western Australian shield, *Nature*, *223*, 701–703.

Freund, R. (1970), Rotation of strike slip faults in Sistan, southeast Iran, *J. Geol.*, *78*(2), 188–200.

Fuller, M. L. (1912), *The New Madrid Earthquake*, vol. 494, U.S. Gov. Print. Off., Wash.

Ghose, S., R. J. Mellors, A. M. Korjenkov, M. W. Hamburger, T. L. Pavlis, G. L. Pavlis, M. Omuraliev, E. Mamyrov, and A. R. Muraliev (1997), The M_S 7.3 1992 Suusamyr, Kyrgyzstan, earthquake in the Tien Shan: 2. Aftershock focal mechanisms and surface deformation, *Bull. Seismol. Soc. Am.*, *87*(1), 23–38.

Goldsworthy, M., J. Jackson, and J. Haines (2002), The continuity of active fault systems in Greece, *Geophys. J. Int.*, *148*(3), 596–618.

Gutiérrez-Santolalla, F., E. Acosta, S. Ríos, J. Guerrero, and P. Lucha (2005), Geomorphology and geochronology of sackung features (uphill-facing scarps) in the Central Spanish Pyrenees, *Geomorphology*, *69*(1), 298–314.

Hauksson, E., L. M. Jones, and K. Hutton (1995), The 1994 Northridge earthquake sequence in California: Seismological and tectonic aspects, *J. Geophys. Res.*, *100*(B7), 12,335–12,355.

Hollingsworth, J., J. Jackson, R. Walker, M. Reza Gheitanchi, and M. Javad Bolourchi (2006), Strike-slip faulting, rotation, and along-strike elongation in the Kopeh Dagh mountains, NE Iran, *Geophys. J. Int.*, *166*(3), 1161–1177.

Jackson, J., and P. Molnar (1990), Active faulting and block rotations in the western Transverse Ranges, California, *J. Geophys. Res.*, *95*(B13), 22,073–22,087.

Johnston, A. C. and L. R. Kanter (1990), Earthquakes in stable continental crust, *Sci. Am.*, 262(3), 68–75.

Johnston, A. C., and E. S. Schweig (1996), The enigma of the New Madrid earthquakes of 1811–1812[1], *Annu. Rev. Earth Planet. Sci.*, *24*(1), 339–384.

Kurdiukov, K. V. (1956), Lypsy reverse fault—Recent displacement of the Earths crust in East Balkhash area, *Proc. Acad. Sci. USSR Geol. Ser.*, *5*, 22–28.

Lee, Y.-H., and Y.-X. Shih (2011), Coseismic displacement, bilateral rupture, and structural characteristics at the southern end of the 1999 Chi-Chi earthquake rupture, central Taiwan, *J. Geophys. Res.*, *116*, B07402, doi:10.1029/2010JB007760.

Liu-Zeng, J., L. Wen, J. Sun, Z. Zhang, G. Hu, X. Xing, L. Zeng, and Q. Xu (2010), Surficial slip and rupture geometry on the Beichuan fault near Hongkou during the Mw 7.9 Wenchuan earthquake, China, *Bull. Seismol. Soc. Am.*, *100*(5B), 2615–2650.
Manighetti, I., M. Campillo, S. Bouley, and F. Cotton (2007), Earthquake scaling, fault segmentation, and structural maturity, *Earth Planet. Sci. Lett.*, *253*(3), 429–438.
McCaffrey, R. (1989), Teleseismic investigation of the January 22, 1988 Tennant Creek, Australia, earthquakes, *Geophys. Res. Lett.*, *16*(5), 413–416.
McKenzie, D., and J. Jackson (1986), A block model of distributed deformation by faulting, *J. Geol. Soc. London*, *143*(2), 349–353.
Mejdahl, V. (1979), Thermoluminescence dating: Beta-dose attenuation in quartz grains, *Archaeometry*, *21*(1), 61–72.
Mikolaichuk, A. V., M. V. Gubrenko, and L. M. Bogomolov (2003), Fold deformations of a preorogenic peneplain in the recent structure of the central Tien Shan, *Geotectonics*, *37*(1), 36–42.
Murray, A. S., and A. G. Wintle (2000), Luminescence dating of quartz using an improved single-aliquot regenerative-dose protocol, *Radiat. Meas.*, *32*(1), 57–73.
Mushketov, I. V., and A. P. Orlov (1893), *Catalog of Earthquakes of the Russian Empire*, Imperial Academy of Sciences St. Petersburg.
Mushketov, O. (1785), Beitrage zur Topographie des Russishen Reiches. 3804.
Nelson, M. R., R. McCaffrey, and P. Molnar (1987), Source parameters for 11 earthquakes in the Tien Shan, central Asia, determined by P and SH waveform inversion, *J. Geophys. Res.*, *92*(B12), 12,629–12,648.
Nur, A., H. Ron, and O. Scotti (1986), Fault mechanics and the kinematics of block rotations, *Geology*, *14*(9), 746–749.
Oglesby, D. D., R. J. Archuleta, and S. B. Nielsen (1998), Earthquakes on dipping faults: The effects of broken symmetry, *Science*, *280*(5366), 1055–1059.
Prescott, J. R., and J. T. Hutton (1994), Cosmic ray contributions to dose rates for luminescence and ESR dating: Large depths and long-term time variations, *Radiat. Meas.*, *23*(2), 497–500.
Rajendran, K., C. P. Rajendran, M. Thakkar, and M. P. Tuttle (2001), The 2001 Kutch (Bhuj) earthquake: Coseismic surface features and their significance, *Curr. Sci.*, *80*(11), 1397–1405.
Reimer, P. J., et al. (2013), IntCal13 and Marine13 radiocarbon age calibration curves 0–50,000 years cal BP, *Radiocarbon*, *55*(4), 1869–1887.
Ron, H., R. Freund, Z. Garfunkel, and A. Nur (1984), Block rotation by strike-slip faulting: Structural and paleomagnetic evidence, *J. Geophys. Res.*, *89*(B7), 6256–6270.
Sala, R., and J.-M. Deom (2005), *Petroglyphs of South Kazakhstan*, Laboratory of Geoarchaeology, Almaty, Kazakhstan.
Savage, J. C., and L. M. Hastie (1966), Surface deformation associated with dip-slip faulting, *J. Geophys. Res.*, *71*(20), 4897–4904, doi:10.1029/JZ071i020p04897.
Schmidt, D. A., and R. Bürgmann (2006), InSAR constraints on the source parameters of the 2001 Bhuj earthquake, *Geophys. Res. Lett.*, *33*, L02315, doi:10.1029/2005GL025109.
Scholz, C. H. (1982), Scaling laws for large earthquakes: Consequences for physical models, *Bull. Seismol. Soc. Am.*, *72*(1), 1–14.
Schulte, S. M., and W. D. Mooney (2005), An updated global earthquake catalogue for stable continental regions: Reassessing the correlation with ancient rifts, *Geophys. J. Int.*, *161*(3), 707–721.
Seeber, L., G. Ekström, S. K. Jain, C. V. R. Murty, N. Chandak, and J. G. Armbruster (1996), The 1993 Killari earthquake in central India: A new fault in Mesozoic basalt flows?, *J. Geophys. Res.*, *101*(B4), 8543–8560.
Selander, J., M. Oskin, C. Ormukov, and K. Abdrakhmatov (2012), Inherited strike-slip faults as an origin for basement-cored uplifts: Example of the Kungey and Zailiskey ranges, northern Tian Shan, *Tectonics*, *31*, TC4026, doi:10.1029/2011TC003002.
Sloan, R. A., J. A. Jackson, D. McKenzie, and K. Priestley (2011), Earthquake depth distributions in central Asia, and their relations with lithosphere thickness, shortening and extension, *Geophys. J. Int.*, *185*(1), 1–29.
Stein, R. S., and G. C. P. King (1984), Seismic potential revealed by surface folding: 1983 Coalinga, California, earthquake, *Science*, *224*(4651), 869–872.
Suvorov, A. I. (1963), Main faults of Kazakhstan and Central Asia (in Russian), in faults and horizontal movements of the Earth's crust, *Trans. Geol. Inst.*, *80*, 173–237.
Suvorov, A. I. (1973), *Deep Faults of Platforms and Geosynclines (in Russian)*, 213 pp., Nedra, Moscow.
Sykes, L. R. (1978), Intraplate seismicity, reactivation of preexisting zones of weakness, alkaline magmatism, and other tectonism postdating continental fragmentation, *Rev. Geophys.*, *16*(4), 621–688.
Tapponnier, P., and P. Molnar (1979), Active faulting and Cenozoic tectonics of the Tien Shan, Mongolia, and Baykal regions, *J. Geophys. Res.*, *84*, 3425–3459.
Thomas, J. C., P. R. Cobbold, A. Wright, and D. Gapais (1996), Cenozoic tectonics of the Tadzhik depression, central Asia, in *World and Regional Geology*, pp. 191–207, Cambridge Univ. Press, New York.
Thompson, S. C., R. J. Weldon, C. M. Rubin, K. Abdrakhmatov, P. Molnar, and G. W. Berger (2002), Late Quaternary slip rates across the central Tien Shan, Kyrgyzstan, central Asia, *J. Geophys. Res.*, *107*(B9), 2203, doi:10.1029/2001JB000596.
Trifonov, V. G. (1978), Late Quaternary tectonic movements of western and central Asia, *Geol. Soc. Am. Bull.*, *89*(7), 1059–1072.
Varnes, D. J., D. H. Radbruch-Hall, and W. Z. Savage (1989), Topographic and structural conditions in areas of gravitational spreading of ridges in the western United States, *U. S. Geol. Surv. Prof. Pap.*, *1496*, 1–28.
Voitovich, V. S. (1969), Nature of the Dzungarian deep fault (in Russian), *Trans. Geol. Inst.*, *183*, 189.
Walker, R., and J. Jackson (2004), Active tectonics and late Cenozoic strain distribution in central and eastern Iran, *Tectonics*, *23*, TC5010, doi:10.1029/2003TC001529.
Walker, R., J. Jackson, and C. Baker (2004), Active faulting and seismicity of the Dasht-e-Bayaz region, eastern Iran, *Geophys. J. Int.*, *157*(1), 265–282.
Walker, R. T., E. Molor, M. Fox, and A. Bayasgalan (2008), Active tectonics of an apparently aseismic region: Distributed active strike-slip faulting in the Hangay Mountains of central Mongolia, *Geophys. J. Int.*, *174*(3), 1121–1137.
Walker, R. T., et al. (2013), The 2010–2011 South Rigan (Baluchestan) earthquake sequence and its implications for distributed deformation and earthquake hazard in southeast Iran, *Geophys. J. Int.*, *193*(1), 349–374.
Walker, R. T., K. W. Wegmann, A. Bayasgalan, R. J. Carson, J. Elliott, M. Fox, E. Nissen, R. A. Sloan, J. M. Williams, and E. Wright (2015), The Egiin Davaa prehistoric rupture, central Mongolia: A large-magnitude normal-faulting earthquake, on a reactivated fault with little cumulative slip, in a slowly-deforming intraplate setting, Geol. Soc. Spec. Publ.: Seismicity, Fault Rupture, and Earthquake Hazards in Slowly deforming regions.
Wallace, R. E. (1989), Fault-plane segmentation in brittle crust and anisotropy in loading system, *Proceedings of Conference XLV; A Workshop on Fault Segmentation and Controls of Rupture Initiation and Termination*, 400–408, Palm Springs, Calif.
Wells, D. L., and K. J. Coppersmith (1994), New empirical relationships among magnitude, rupture length, rupture width, rupture area, and surface displacement, *Bull. Seismol. Soc. Am.*, *84*(4), 974–1002.

Wesnousky, S. G. (2005), Active faulting in the walker lane, *Tectonics*, *24*, TC3009, doi:10.1029/2004TC001645.
Wintle, A. G., and A. S. Murray (2006), A review of quartz optically stimulated luminescence characteristics and their relevance in single-aliquot regeneration dating protocols, *Radiat. Meas.*, *41*(4), 369–391.
Xu, X., X. Wen, G. Yu, G. Chen, Y. Klinger, J. Hubbard, and J. Shaw (2009), Coseismic reverse-and oblique-slip surface faulting generated by the 2008 M_w 7.9 Wenchuan earthquake, China, *Geology*, *37*(6), 515–518.
Yielding, G., J. A. Jackson, G. C. P. King, H. Sinvhal, C. Vita-Finzi, and R. Wood (1981), Relations between surface deformation, fault geometry, seismicity, and rupture characteristics during the El Asnam (Algeria) earthquake of 10 October 1980, *Earth Planet. Sci. Lett.*, *56*, 287–304.
Zimmerman, D. W. (1971), Thermoluminescent dating using fine grains from pottery, *Archaeometry*, *13*(1), 29–52.
Zischinsky, U., et al. (1966), On the deformation of high slopes, in *Proceedings, First Congress of the International Society of Rock Mechanics*, vol. 2, pp. 179–185, Lisbon, Portugal.
Zubovich, A. V., et al. (2010), GPS velocity field for the Tien Shan and surrounding regions, *Tectonics*, *29*, TC6014, doi:10.1029/2010TC002772.